Investigation of Neutronics and Heat Transfer in a Gas Core Reactor

Gert Jan Auwerda

Supervisor:
Danny Lathouwers

PNR-131-2009-004

February 11, 2009

Abstract

A gas core reactor (GCR) is a nuclear reactor in which the fuel is in a gaseous state inside the core. The most important characteristic of a GCR is that there are no constraints on the fuel temperature because the fuel is a gas and cannot melt or vaporize. Because of this, GCRs have potentially the highest core temperature of all existing and proposed reactor designs, with fuel temperatures in the thousands of Kelvins, which significantly increases the efficiency of the power conversion cycle.

The neutronics and heat transfer in a GCR were investigated using a one-dimensional cylindrical core model with stationary fuel. The fuel gas consisted of a mixture of uranium- and carbon-fluorides in thermal equilibrium with a graphite reflector wall at 2000 K. Critical densities were calculated using both 50% and 5% enriched uranium as well as reactivity coefficients for the fuel density, fuel temperature and reflector temperature. To calculate the radial temperature and density profiles in the core a heat transfer code was developed, including dissociation of the fuel gas and both radiative and kinetic heat transfer. Coupled neutronics and heat transfer calculations were performed to investigate the effects of changes in the fuel and temperature profiles on the neutronics, and of accurate calculation of the specific power density on the heat transfer.

The reactivity coefficient of the fuel density and of the reflector temperature are both large in a GCR, but reactor control depends mostly on the first, as feedback from the reflector will be delayed due to its large mass and the low thermal conductivity of the fuel gas near the wall. The fuel temperature reactivity coefficient will have a secondary role as it is relatively small. Due to the large reactivity coefficient of the fuel density, density fluctuations may cause large reactivity insertions in a GCR. Dissociation and kinetic heat transfer both play an important role in the heat transfer in a GCR, having a significant effect on the pressure, average fuel temperature, fuel redistribution towards the wall and heat transfer near the wall. The coupled calculations show that a flat neutron flux can be used in heat transfer calculations and that the radial density and temperature profiles in a GCR have no effect on the reactivity when using low enriched fuel.

Nomenclature

GCR   Gas Core Reactor.

LWR   Light Water Reactor

MHD   Magnetohydrodynamic.

UCF gas   Uranium-Carbon-Fluoride gas.

VCR   Vapor Core Reactor.

α'_n Normalized reactivity coefficient of the fuel density.

α_{Tf} Reactivity coefficient of the fuel temperature [pcm/K].

α_{Tr} Reactivity coefficient of the reflecor temperature [pcm/K].

$A_{i+\frac{1}{2}}$ Area of interface between cells i and $i+1$ [m^2].

c Speed of light [m/s].

c_p Heat capacity [J/kgK].

D_r Radiative diffusion constant [m^2/s].

$f(r)$ Specific power density [W/kg uranium].

f_C Carbon atom ratio in the fuel gas.

f_F Fluoride atom ratio in the fuel gas.

f_U Uranium atom ratio in the fuel gas.

g Dissociation function.

k Boltzmann constant [J/K].

k_{eff} Neutron multiplication factor.

λ_{graph} Graphite thermal conductivity [W/mK]

λ_{int} Internal thermal conductivity [W/mK].

λ_{kin} Kinetic thermal conductivity [W/mK].

λ_{react} Reactant thermal conductivity [W/mK].

λ_r Radiative thermal conductivity [W/mK].

λ_{tot} Total thermal conductivity [W/mK].

λ_{tr} Translational thermal conductivity [W/mK].

l_a Neutron mean-free-path length for absorption [m].

l_{ph} Photon mean-free-path length [m].

l_s Neutron mean-free-path length for scattering [m].

l_t Total neutron mean-free-path length [m].

m Number of fine cells per course volume zone in the Heat Transfer code.

m_U Atomic mass of uranium [kg].

n Molecular fuel gas density [molecules/m^3].

N_0 Number of original molecules in the system.

n_0 Particle density without dissociation [molecules/m3].

n_c Critical fuel gas density [atoms/barn-cm].

n_f Atomic fuel gas density [atoms/barn-cm].

$n_U(r)$ Uranium atom density [atoms/m^3].

P Power generated in the reactor core [W].

p Pressure [Pa].

$\vec{q}$ Heat flux [W/m^2].

$\vec{q}_r$ Radiative heat flux [W/m^2].

$Q(r)$ Power density [W/m^3].

ΔR_i Width of course volume zone i.

Δr_i Width of volume cell i [m].

$\rho(r)$ Fuel gas density [kg/m^3].

$\rho_U(r)$ Uranium density [kg/m^3].

R Universal gas constant [J/molK].

r Radial coordinate in the core [m].

R_c GCR core cavity radius [cm].

R_r Reflector thickness [cm].

Σ Macroscopic cross section [m^{-1}].

σ_{ph} Microscopic photon collision cross section [m^2].

σ_{SB} Stefan-Boltzman constant [W/m^{2}K^4].

$\widetilde{T}$ Effective temperature [K].

$T(r)$ Fuel temperature [K].

T_f Average fuel gas temperature [K].

T_{max} Maximum fuel gas temperature [K].

T_r Average reflector temperature [K].

T_{wall} Inner wall temperature of the graphite reflector [K].

u Radiative density [J/m^3].

V Volume [m^3].

V_i Volume of volume cell i [m^3].

W_0 Average weight per molecule without dissociation [kg].

Contents

Chapter 1

Introduction

1.1 General Introduction

A gas or vapor core reactor (GCR/VCR) is a nuclear fission reactor in which the fuel is in a gaseous state inside the core. The core consists of a cavity, filled with the fuel gas, surrounded by a reflector. The fuel gas usually consists of UF_4, but designs with higher fluoride fractions exist. At high core temperatures, above 10000 K, a high level of ionization can be realized in the fuel gas, and it becomes a plasma. These type of reactors are sometimes called plasma core reactors.

The most important characteristic of a GCR is that, because the fuel is in a gaseous state, there are no constraints on the fuel temperature. It cannot rupture, melt, vaporize or be destroyed. The only constraints on the temperature are those imposed by the reactor vessel, which are far less severe than the constraints that normally apply to the fuel. Because of this GCRs have potentially the highest core temperature of all existing and proposed reactor designs.

The main benefit of a GCR is its high operating temperature, which increases the efficiency of the conversion from thermal heat to electricity, and also the efficiency of hydrogen production methods [Brown,2002]. One of the most interesting features of a GCR comes from the fuel ionization, which makes it possible to convert part of the thermal energy in the fuel gas directly to electricity, for example through magnetohydrodymanic (MHD) power conversion, further increasing the efficiency of the electricity production.

Additional advantages of a GCR include very high maximum fuel burnup of over 500 GWD/MTU, and very low waste production due to efficient moderation of neutrons, resulting in a lower production of higher actinides. The efficient moderation of neutrons in a GCR also results in lower plutonium buildup which, combined with efficient fissioning of fissionable plutonium isotopes, results in excellent proliferation resistance [Anghaie,2005]. Furthermore the low fuel inventory in a GCR, one or two orders lower compared to a conventional light water reactor (LWR), means a lower safety risk in the case of accidents, because less radioactive material is present. Due to the large power density inside a GCR core, possible utilization besides normal power production is in space crafts, both as part of the propulsion system and as (electrical) power source [Diaz,1993, Dugan,1989, Dugan,1993].

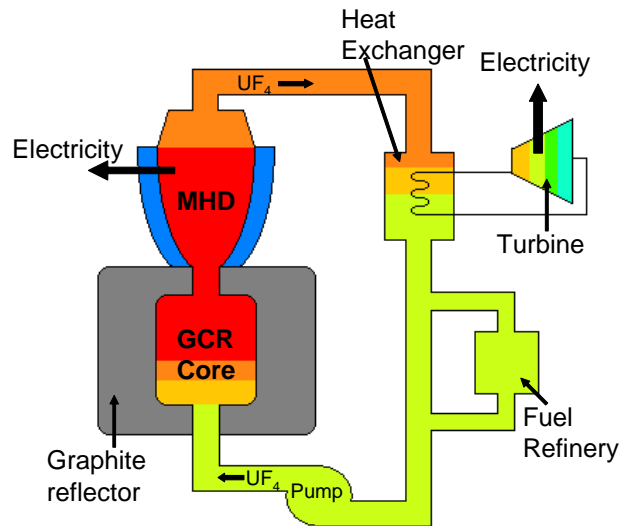A conceptual design of a GCR power plant is shown in figure 1.1. In this

Figure 1.1: Gas core reactor (GCR) design with direct energy conversion using an MHD convertor and a closed fuel loop.

design the GCR core consists of a cavity surrounded by a graphite reflector. The fuel is circulated through a closed loop. Inside the core the fuel is heated up, and is then lead through an MHD device to convert part of its energy directly to electricity. The remaining heat is extracted in a heat exchanger and converted to electricity using conventional methods. A fuel refinery is included in the loop, which allows online refuelling of the reactor and in which fission products can be removed from the fuel gas.

In a Gen IV roadmap presentation regarding non-classical systems it was stated that: "Gas/vapor core reactors set the upper performance potential in sustainability and safety with no insurmountable technology challenge". This 'no insurmountable challenge' is in reality 'nearly insurmountable' though. Using fuel in a gaseous state means density fluctuations could arise inside the core, which could cause stability problems for the reactor power. Futhermore, to attain a high enough level of ionization to make direct energy convergence efficient, high temperatures are needed, combined with a high neutron flux to increase the ionization of the fuel [Bitteker,1993]. This means the MHD power convertor, a complicated electromagnetic device, needs to be capable of handling extremely high temperatures as well as a high radiation level. Finally, not only need the walls of a GCR reactor core to be able to withstand high temperatures of over 2000 K, they also need to be resistant to radiation and to corrosion due to the fluoride in the fuel gas.

1.2 Overview of the work

In most research on gas core reactors, either the neutronics in a GCR are calculated, assuming uniform temperature and density distributions [Dugan,1993], or the heat transfer is investigated, assuming a uniform flux distribution [Diaz,1993]. The motivation to these assumptions is that the fuel density inside the core is low, and therefore the neutron mean-free-path length is large compared to the geometry. Thus, fluctuations in space are assumed to be negligible, as neutrons only see the 'average' value inside the core. Because of these large neutron mean-free-path lengths, the flux is also assumed flat, and the power density is taken to be directly proportional to the uranium density inside the core. The error made in making these assumptions is expected to be small, but rarely quantified.

This research was performed as a master end project (MEP) in the field of applied physics at the technical university of Delft, in the physics of nuclear reactors (PNR) department. Research was performed on a graphite-walled GCR with the fuel gas consisting of a mixture of uranium- and carbon-fluorides in thermochemical equilibrium with the graphite wall. This design was first proposed by Kistemaker [1978] as a solution to the incompatibility of most wall materials with the high temperatures and corrosive effects of the uranium-fluoride fuel gas, and was later the subject of PhD researches by Klein [1987] and Kuijper [1992]. A one-dimensional core design was used of an infinite cylinder, and fuel flow was ignored to keep the project manageable inside the allocated timeframe. The main goal of this research is quantifying the effect of coupled neutronics and heat transfer calculations, as opposed to doing uncoupled calculations, assuming flat temperature, density and flux distributions. This was also done as preparation for transient calculations in a GCR, where the interaction of the fuel density and temperature with the neutronics is of importance. To further investigate the transient behaviour, and to be able to put the effect of the density and temperature distribution on the reactivity in perspective, other reactivity effects in a GCR were also calculated.

The research followed the same lines as a paper by van Dam and Hoogenboom [1983] dealing with one-dimensional GCR core designs. In this paper the main parameters governing the neutronics and heat transfer were investigated, dealing first with the neutronics and heat transfer separately, followed by a synthesis that investigated the effects of the fuel redistribution inside the core on the reactivity.

This thesis starts with detailing the investigated core models in the first section of chapter 2. The first core model is identical to the cylindrical core design from van Dam and Hoogenboom and is used as a reference case to verify the calculations. In this model high enriched (50%) uranium was used. Such a high enrichment is no longer realistic due to the high cost of high enriched uranium. Using two other models the reference case was altered in two steps to a core model fuelled with low enriched (5%) uranium. The rest of the chapter describes the neutronic calculations, assuming a flat temperature and density distribution inside the core. For each core case first the critical density was calculated, and next the important reactivity coefficients near criticality were calculated as well as the neutron mean-free-path length and specific power density. The chapter concludes with a discussion on the possible impact of the calculated reactivity coefficients on the stability of the three GCR core cases.

9

In chapter 3 a heat transfer model was developed including both radiative and kinetic (conductive) heat transfer. Dissociation of the large fuel gas molecules into smaller ones at higher temperatures was included, as it was expected to have a major effect on the density distribution inside a GCR. Again calculations were validated against previous calculations by van Dam and Hoogenboom [1983], which did not include dissociation and kinetic heat transfer. With the heat transfer model tested and validated, it could be used to calculate the temperature and density profiles inside the three core cases, as well as several other parameters like core pressure, maximum temperature and heat loss through the graphite wall. The only coupling with the neutronics in this chapter was the use of the average fuel gas density at criticality, calculated in chapter 2.

In the fourth chapter, neutronics and heat transfer calculations were combined. The effect of the neutron flux distribution on the heat production and on the temperature and density distribution was investigated, and the effect of fuel redistribution and the temperature distribution inside a GCR on the reactivity was determined. Results were compared with results in [van Dam,1983] for the reference core model, and with results from the uncoupled calculations from chapters 2 and 3.

Finally, chapter 5 gives the conclusions drawn on the important parameters for the neutronics and heat transfer inside a GCR, the effect of the temperature and density profiles on the neutronics and the other way around, and the transient behaviour of a GCR. The conclusions are followed by a discussion on the validity of the results, including limitations of the models used, and recommendations for future work.

Chapter 2

Neutronics analysis with uniform temperature and density distribution

Models using uniform temperature and mass distributions inside the core are often used in studies of the neutronics of a GCR [Anghaie,2005, Dugan,1989, Dugan,1993]. The effects of spatial fuel density and temperature variations on the neutronics are expected to be minor, due to the large neutron mean-free-path lengths inside a GCR core. To investigate the validity of these assumptions, results on the neutronics for uniform temperature and density distributions are needed as a reference. For comparison of the possible effects of fuel redistribution, and as a preliminary investigation in the transient behaviour of a GCR, reactivity coefficients of various properties of a GCR are also calculated.

The neutronics of a gas core reactor are investigated using a one-dimensional cylindrical core model, detailed in section 2.1, with uniform mass and temperature distribution of the fuel inside the core, and a uniform reflector temperature. Three different core setups are investigated; a reference case with high enriched uranium (50%) from van Dam and Hoogenboom [1983], a second high enriched case with lower fuel temperature, and one with low enriched uranium (5%). With MCNP [Los Alamos,2003] first the critical fuel density is calculated for each core, and for this critical density the neutron mean-free-path lengths are calculated and the specific power density inside the cores is determined. Also, reactivity coefficients near criticality for the fuel temperature, the reflector temperature, and the fuel density are calculated in paragraphs 2.3.4 to 2.3.6. All results are compared with values from van Dam and Hoogenboom, and with each other. In the final section a discussion is held on possible stability issues for GCRs, given the calculated feedbacks.

2.1 Investigated Core Models

In this section the geometry and properties of the three different GCR core models investigated in this thesis are detailed. For all three core cases a one-dimensional model was used of an infinite cylinder, without axial or tangential
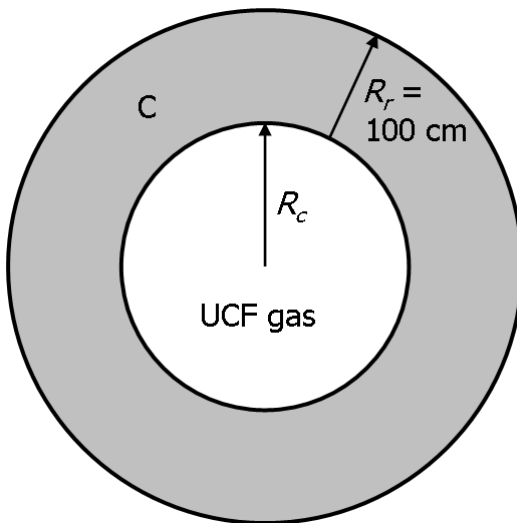
Figure 2.1: Geometry of the GCR model, consisting of an infinite cylinder with a core cavity with radius R_c filled with UCF gas, encircled by a graphite reflector with thickness $R_r = 100$ cm.

dependence, consisting of a cylindrical cavity filled with a fuel gas mixture of uranium- and carbon-fluorides (UCF gas), surrounded by a cylindrical graphite reflector. Both the fuel gas and the graphite reflector had a uniform density and temperature. A cross-section of this model is depicted in figure 2.1. For all three cases, the graphite of the reflector has a density of 0.0855 atoms/barn-cm, or 1705 kg/m^3 [Kuijper,1992], and is 100 cm thick ($R_r = 100$ cm).

The three different core setups, labelled cases 1 to 3, listed in table 2.1, differ in their inner core radius R_c, fuel gas mixture, uranium enrichment, fuel temperature T_f and reflector temperature T_r. Altough the reflector inner wall temperature was assumed to be always 2000 K, the actual reflector temperature T_r refers to the average bulk temperature of the reflector. Since the thermal neutron diffusion length in graphite is large (~ 60 cm), the neutron temperature is assumed to be mainly determined by the bulk of the graphite.

The first case is identical to the cylindrical core model in van Dam and Hoogenboom [1983], in which the neutronics of several one dimensional GCR models were investigated. To test the calculation methods against results reported in van Dam and Hoogenboom, calculations were performed on a cylindrical GCR with properties identical to those in van Dam and Hoogenboom. This reference core has an inner radius of $R_c = 118$ cm and the fuel gas consists of 70% UF$_4$ and 30% CF$_4$ molar fractions with 50% enriched uranium. The fuel has a uniform temperature of $T_f = 10000$ K and the reflector temperature is $T_r = 1000$ K.

The two other cases have a uniform fuel temperature of $T_f = 4400$ K, a uniform reflector temperature of $T_r = 1900$ K and an inner core radius of $R_c = 150$ cm. Case 2 uses fuel with 50% enriched uranium, and case 3 5% enriched uranium. There properties were chosen such that case 2 could serve as a link between the reference case 1 and case 3, with a more realistic uranium

Table 2.1: The three different investigated core setups. For each case the atom ratios U:C:F of the fuel mixture, the uranium enrichment percentage, the inner core radius R_c, core temperature T_f and reflector temperature T_r is given. The reflector thickness $R_r = 100$ cm in all cases.

	Fuel mixture [U:C:F]	Fuel Enrichment [% ^{235}U]	R_c [cm]	T_f [K]	T_r [K]
Case 1	0.70 : 0.30 : 4.00	50%	118	10000	1000
Case 2	0.70 : 0.18 : 4.00	50%	150	4400	1900
Case 3	0.70 : 0.18 : 4.00	5%	150	4400	1900

enrichment for modern reactors. For case 2 and 3 the fuel gas consists of a mixture of U:C:F atoms with atom ratios U:C:F of 0.70 : 0.18 : 4.00. The mixture was chosen such that at a temperature of 2000 K at the wall and a gas pressure of 25 bar it would be in chemical equilibrium with the graphite wall, as described in Klein [1991a]. The fuel temperature was limited to 4400 K because calculations using the heat tranfer model desribed in chapter 3 showed higher average fuel temperatures would result in pressures above 100 bars for the low enriched fuel at critical fuel density, beyond the boundaries of the validity of the data used in the heat transfer model. For the same reason the core radius was enlarged to 150 cm. A slightly different fuel mixture than for case 1 was chosen because for this fuel mixture detailed thermodynamical data was avaiable from Klein [1991a, 1991b]. The reflector temperature was chosen based on heat transfer calculations for a critical core, which resulted in an average reflector temperature of around 1900 K, based on an inner reflector wall temperature of 2000 K. See table 2.1 for an overview of the three core setups.

2.2 Calculation Method

All neutronics calculations were performed using the MCNP5 Monte Carlo transport code [Los Alamos,2003]. MCNP is a Monte Carlo code, and as such results depend on statistics of random events. A benefit of using MCNP is that it describes very accurately the physics of the problem, and reports a standard deviation with all calculated values, which can be difficult to estimate when using a deterministic method. MCNP is continuous in space and energy, using point-wise cross section data. Also, no cross section libraries have to be evaluated as MCNP can internally evaluate cross sections at different temperatures. A drawback of using MCNP is that the statistical error in the results makes the calculation of small changes in the system difficult, like the calculation of reactivity coefficients. At the start of this project, it was not clear that feedbacks on the reactivity would be included, and as such MCNP was chosen in favor of a deterministic code, because of its ease of use and precision.

In all neutronics calculations in this research the multiplication factor k_{eff} was calculated using a `KCODE` card in the MCNP input deck, and sometimes tallies were included to evaluate other neutronics related quantities. Neutron energies were split up into 4 groups with upper energy bounds of 2.38 eV, 4.3 keV, 111 keV and 20 MeV, equal to the groups used in van Dam and Hoogenboom [1983]. A sample MCNP input deck is given in appendix A.

2.3 Calculation Results

2.3.1 Critical Density

For each core case, the critical fuel gas density n_c (the density for which $k_{eff} = 1$) had to be evaluated before other calculations could be performed. The critical densities are given in total atom densities of the fuel gas, and are the sum of the atom densities of the seperate components, with units in atoms/barn-cm, equal to the input format in MCNP. The atom densities of the seperate components of the fuel gas can be evaluated from this total density using their atomic ratios given in table 2.1. With f_U, f_C and f_F the atom ratios of the fuel gas components, the uranium atom density n_U in atoms/m^3 can be calculated from the critical density n_c by

$$ n_U = \frac{f_U}{f_U + f_C + f_F} n_c \times 10^{30} \tag{2.1} $$

where multiplication by the factor 10^{30} is needed to convert the densities from (barn-cm)$^{-1}$ to m^{-3}.

Without dissociation, it is assumed all fluoride atoms are bound to uranium or carbon atoms, forming UF$_4$, UF$_5$ or UC$_4$ molecules. The molecular fuel density or particle density n in molecules/m^3, needed to calculate the pressure, can be evaluated, ignoring dissociation, from the critical density by

$$ n = n_U + n_C = \frac{f_U + f_C}{f_U + f_C + f_F} n_c \times 10^{30} \tag{2.2} $$

From the molecular fuel density n, the core pressure p, ignoring dissociation, for the critical fuel density and fuel temperature T_f, can be calculated using the ideal gas law by

$$ p = nkT_f \tag{2.3} $$

with k the Boltzmann constant.

For case 1, n_c could be directly evaluated from results in van Dam and Hoogenboom [1983] calculated with the ANISN deterministic S_n code, which used cross section libraries created for the fuel gas mixture at the fuel gas temperature of 10000 K. The critical inventory was given as 7.65 kg uranium per meter length of the cylinder, translating to a UCF fuel gas density of $n_c = 3.18 \times 10^{-5}$ atoms/barn-cm, using data from Lide [2001] for atomic weights and physical constants. For the other two core cases, the critical density n_c was determined from several MCNP criticality calculations for a range of fuel gas densities. After making a linear fit on the calculated data points, n_c was determined from the intersection of the fit with $k_{eff} = 1$. For plots of these calculations and the linear fits see figure 2.3.

For all cases, using the calculated critical fuel gas density n_c as input, a long MCNP run was done of 1000 cycles with 75000 source particles, to calculate the k_{eff} belonging to this fuel density with high precision, since this k_{eff} value will be used as a reference case for various perturbations in the rest of this research. The calculated k_{eff} values has a standard deviation of 9 pcm (10^{-5}). Results are given in table 2.2.

Results for the reference case, case 1, are in accordance with van Dam and Hoogenboom. Using the critical inventory reported in van Dam and Hoogenboom, the calculated multiplication factor was within one standard deviation of

Table 2.2: Critical fuel densities n_c for each case. Using this n_c as input, k_{eff} was calculated with MCNP, with a standard deviation of 9 pcm. Also given is the total mass of uranium in kg per meter length of the cylinder and the resulting gas pressure p, ignoring dissociation of the fuel gas, given the critical fuel gas density and fuel temperature.

	n_c [atoms/b-cm]	k_{eff}	Critical Inventory [U kg/m]	p [bar]
Case 1	3.180×10^{-5}	1.00009	7.65	8.78
Case 2	2.833×10^{-5}	0.99994	11.3	3.10
Case 3	4.370×10^{-4}	1.00019	175	47.9

criticality. The pressure difference of 0.07 bar between van Dam and Hoogenboom and the calculated value is due to rounding errors of various numbers. This result gives confidence in the correct sampling of cross sections by MCNP for temperatures in the thousands of Kelvin.

The second case, with the same uranium enrichment as case 1, has a larger critical inventory due to a higher reflector temperature. This results in a harder thermal neutron spectrum, reducing the effective absorption cross section in the fuel, which has to be compensated for by adding more fuel. The critical density n_c is still lower than for case 1, because of the larger core radius. Finally, the critical density for the low enriched fuel, case 3, is over ten times as high as for the high enriched fuel, to compensate for the lower fissile ^{235}U fraction and the additional absorption in ^{238}U due to an increase in the ^{238}U density.

2.3.2 Neutron Mean-Free-Path Lengths

The neutron mean-free-path length inside a GCR core is an important property to understand its neutronic behaviour. It is usually assumed that the mean-free-path of neutrons inside a GCR core is much larger than the core diameter, and that neutrons have a higher probability to be absorbed than to scatter in the fuel, and as a result neutrons can be assumed to travel in straight, uninterrupted lines through the core. To be able to test the validity of certain assumptions regarding the mean-free-path lengths and the ratio between neutron absorption and scattering, the mean-free-path lengths for scattering l_s, absorption (including fission) l_a, and total l_t for thermal neutrons inside the three GCR core were calculated for each core case using MCNP.

In MCNP, reaction rate tallies in the fuel were calculated for the scattering, absorption and total cross-sections, and for the flux, for the four neutron energy groups described in section 2.2. Since we were only interested in the thermal neutron mean-free-path lengths, we only looked at the results for the thermal energy group with neutron energy $E < 2.38$ eV. The macroscopic cross section Σ_i for each reaction i can be calculated from the thermal group reaction rates RR_i and thermal flux ϕ by

$$\Sigma_i = \frac{RR_i}{\phi} \tag{2.4}$$

where i indicates the type of reaction (a for absorption, s for scattering and t for total). From Σ_i the thermal neutron mean-free-path lengths l_i are calculated

Table 2.3: Thermal ($E < 2.38$ eV) neutron mean-free-path lengths inside the GCR reactor cores. For each core case the mean-free-path length for absorption (including fission) l_a, scattering l_s, and the total mean-free-path length l_t is given.

	n_c [atoms/b-cm]	l_a [m]	l_s [m]	l_t [m]
Case 1	3.180×10^{-5}	17.0	56.9	13.1
Case 2	2.833×10^{-5}	26.7	70.5	19.3
Case 3	4.370×10^{-4}	16.7	4.9	3.8

by

$$l_i = \frac{1}{\Sigma_i} \tag{2.5}$$

Results for the scattering, absorption and total mean-free-path lengths l_s, l_a and l_t for thermal neutrons with neutron energy $E < 2.38$ eV are given in table 2.3 for each case.

The calculated mean-free-path for absorption $l_a = 17.0$ m for case 1 is equal to the value given in van Dam and Hoogenboom of $l_a \sim 17$ m, for a spherical GCR with identical fuel and the same reflector temperature. The calculated mean-free-path lengths for core case 1 are smaller than for case 2. In part this is because of the higher fuel gas density in case 1, but another important reason is the lower reflector temperature for case 1. As discussed before this results in a shift of the thermal neutron peak towards a slightly lower energy, where both the absorption and scattering cross sections have higher values. Since the calculated mean-free-path lengths are for thermal neutrons, the fuel temperature T_f has no significant effect on them, because there are no resonances in the cross sections in the thermal energy region. When comparing the l's for case 1 and case 2 with the core diameters, they both have comparable mfp lengths compared to their core diameters R_c. Since $l_t \gg R_c$ for case 1 and 2, and since $l_a \ll l_s$, the assumption of neutrons traveling through the core in straight, uninterrupted lines is reasonable for these cases.

Case 3 shows a smaller l_a than case 2, mostly due to a slightly higher ^{235}U density. The much higher ^{238}U density has only a small effect on l_a, because the fission cross-section of ^{235}U is several orders larger than the absorption cross section of ^{238}U in the thermal region. Thus l_a is dominated by fission of ^{235}U. l_s is much smaller for case 3 than for the other cases, because of the higher fuel density. As a result, in case 3 $l_s > l_a$, and the total mean-free-path length l_t is comparable to the core diameter instead of being several orders larger. Thus for case 3 the assumptions of neutrons traveling through the core in straight lines is no longer accurate.

2.3.3   Specific Power Density

For the calculation of the heat generation inside the core in chapter 3, a quantity was needed that described the power production per kg uranium as a function of the radial position r inside the core. Based on the defenition of the specific
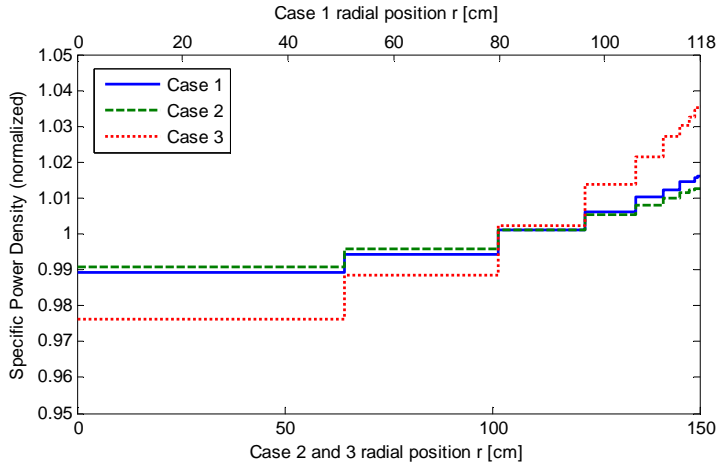
Figure 2.2: Normalized specific power density $f(r)$ of the three cases. The r-coordinate of case 1 is depicted on the top x-axis, the values on the bottom x-axis refer to the r-coordinates of cases 2 and 3.

power of a nuclear reactor [Duderstadt,1976]

$$Specific\ power\ [\text{kW/kg}] = \frac{\text{Reactor thermal power}}{\text{Total mass of fissionable material}} \qquad (2.6)$$

the specific power density $f(r)$ was defined as

$$Specific\ power\ density\ f(r)\ [\text{W/kg}] = \frac{\text{Fisson power density at } r}{\text{Uranium density at } r} \qquad (2.7)$$

For each case the specific power density $f(r)$ was calculated using a type 7 volume tally in MCNP, which calculates the fission energy deposition averaged over a cell, per gram fuel in that cell. The core in the MCNP model was split in 10 radial zones, with smaller zones closer to the reflector. The distribution of the zone widths is explained in section 3.5. The specific power density was calculated for each volume cell and the resulting values were normalized to an average specific power density of 1 for the entire core, such that $\frac{\int_V f(r)\rho_U(r)dV}{\int_V \rho_U(r)dV} = 1$, with $\rho_U(r)$ the uranium density at r. The calculated specific power densities for all three core cases are plotted in figure 2.2.

Because the flux shape is almost flat inside a GCR due to the large mean-free-path length of neutrons compared to the core radius (see appendix C and table 2.3), the power production inside a GCR core can almost always be assumed proportional to the uranium density [van Dam,1983, Kuijper,1992], which means a flat specific power density is assumed. Figure 2.2 shows that this, especially for case 3, is not entirely correct. The difference in specific power density at the centre of the core and near the wall is between 2% (case 2) and 6% (case 3). This indicates a higher fission probability and thus a higher neutron flux near the wall, for which there are two reasons.

First, inside a GCR, due to the large mean-free-path length for neutrons in the fuel, moderation in the fuel is almost absent, and almost all fast neutrons will reach the graphite reflector. Thus, the reflector can be seen as the source of

thermal neutrons. With thermal neutrons entering the core from the reflector, absorption and scattering by the fuel will cause a slight drop of the thermal flux further away from the wall, and thus a slight drop in the specific power density.

Second, as was mentioned in van Dam and Hoogenboom, if we assume neutrons to move in straight, uninterrupted lines through the core, which is a good approximation for cases 1 and 2, where $l_t \gg R_c$ and $l_a \ll l_s$, it can be shown that for neutrons leaving the reflector at random angles, this will result in a larger neutron flux near the wall than near the centre of the core. See appendix B.

When comparing the specific power density of the three cases, case 3 has a greater difference between $f(r)$ at the centre and near the wall than the other two cases. Main reason is the higher fuel gas density (over 10 times higher), resulting in a shorter neutron mean-free-path length, causing less thermal neutrons to reach the centre of the core due to scattering near the wall.

Case 1 and 2 have a nearly identical specific power density, with a slightly larger slope for case 1, due to a higher absorption probability for case 1. This is in part because of the slightly higher fuel density, but the most important factor is that the lower reflector temperature causes a slight shift in the thermal neutron peak towards lower neutron energies. As discussed before, this shift in the thermal neutron energies results in a higher neutron absorption probability in the fuel.

2.3.4   Fuel Density Reactivity Coefficient

Since the fuel is in a gaseous state in a GCR, density fluctuations can easily arise from changes in either the pressure or the temperature. As such, the reactivity coefficient of the fuel is an important property for transients and control of a GCR. The feedback on the reactivity from changes in the fuel density was calculated for the three cases from table 2.1. For each case the multiplication factor k_{eff} was calculated for several fuel densities around the critical density, and a linear fit was made on the calculated data points. For cases 2 and 3 these linear fits were also used to determine the critical fuel density n_c in table 2.2. The slope of the linear fits gave the fuel density feedbacks. Plots of the calculated data points and the linear fits are given in figure 2.3.

The resulting feedbacks are given in table 2.4 and are expressed as the normalized reactivity coefficient of the fuel near criticality, defined by $\alpha'_n = \frac{n_f}{k} \frac{\partial k}{\partial n_f}$, with n_f the atomic fuel density in atoms/barn-cm. The normalized reactivity coefficient of the fuel gives the relative change of k_{eff} (which, near criticality, is equal to the absolute change), per relative change of the fuel density n_f. The main reason for using the normalized reactivity coefficient instead of the (absolute) reactivity coefficient $\alpha_n = \frac{\partial k}{\partial n_f}$, is that trying to express the absolute reactivity coefficient of the fuel in easily readable numbers would result in strange units, and would not be very insightful to the behaviour of the reactor.

In van Dam and Hoogenboom the normalized reactivity coefficient of the fuel was calculated for a spherical GCR of 2 meter radius, with otherwise identical properties as case 1. The calculated normalized reactivity coefficient was $\alpha'_n \simeq 0.28$, which is equal to α'_n calculated for case 1, a cylindrical GCR. Although the geometry of the two cores is different, the rest of the parameters are the same. Given the large mean-free-paths of neutrons inside the core, much larger than the core diameter (see table 2.3), neutrons will enter and exit the reflector several

Table 2.4: Normalized reactivity coefficient of the fuel $\alpha'_n = \frac{n}{k}\frac{\partial k}{\partial n}$ near criticality and the critical fuel density n_c for each case.

	n_c	α'_n
	[atoms/b-cm]	-
Case 1	3.180×10^{-5}	0.28
Case 2	2.833×10^{-5}	0.31
Case 3	4.370×10^{-4}	0.18

times before being absorbed by the fuel, and the neutron energy spectrum will depend only on the reflector properties and be the same for the two geometries. Since the fuel has identical properties, the macroscopic cross sections must also be equal, and the average neutron path length through the core will be equal for the two different geometries (although the distribution between path lengths might be different). Small changes in density would result in equal changes in absorption probabilities for neutrons traveling through the core, resulting in equal reactivity coefficients. Thus the results compare well with literature.

For case 2 the normalized reactivity coefficient of the fuel is slightly larger than for case 1, because of the larger mean-free-path length compared to the core diameter for case 2. Each time neutrons enter the reflector there is a chance they will be absorbed or escape. A relative change in density will cause a relative change in l_a and in the average number of times neutrons will pass the core and enter the reflector. Because l_a/R_c is larger for case 2 than for case 1, an equal relative change in the fuel density for case 2 compared to case 1 will cause a higher absolute change in l_a/R_c and in the average number of times neutrons enter the reflector, and thus will cause a bigger change in k_{eff}. Because of this the reactivity coefficient for the fuel for case 2 is higher than for case 1.

Case 3 has a significantly lower α'_n, which is mainly due to the lower fuel enrichtment, resulting in a competition between absorption in ^{238}U and fission of ^{235}U for thermal neutrons. Because of these two opposite effects on the reactivity a change in the fuel density results in a relative low change of reactivity. Another factor is that at these higher ^{238}U densities, resonance absorption of neutrons in ^{238}U before being moderated is no longer insignificant. Enlarging the fuel density will enlarge the probability of neutrons being absorbed in ^{238}U before being moderated, lowering the efficiency of adding more and more fuel. This effect was also noted in Dugan [1989].

The high reactivity coefficient of the fuel might be a perfect feedback mechanism to control the reactor, as suggested in Dugan, since a temperature rise will cause a pressure rise and thus a density drop. But it might also be the cause of instabilities. For the high enriched cases density changes of only 2% will already result in reactivity changes of 600 pcm, around 1\$ worth of reactivity. For case 3, a density change of 4% will result in such a change in reactivity. A lot of scenarios can be imagined which can cause density fluctuations in the fuel gas of several percent, for example a blockage of the fuel flow upstream of the core, or a fuel pump malfunction. Without proper design, these density changes can cause unstable power fluctuations due to the strong feedback.
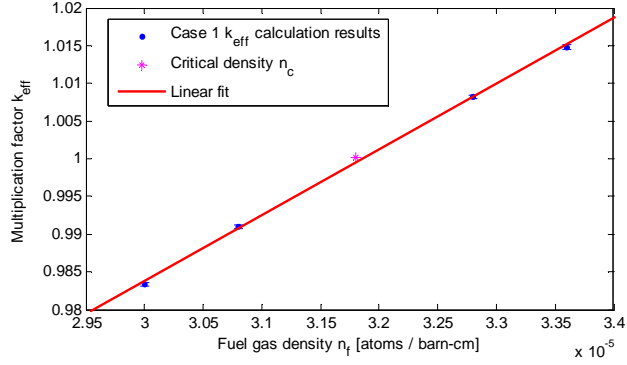
(a) Case 1
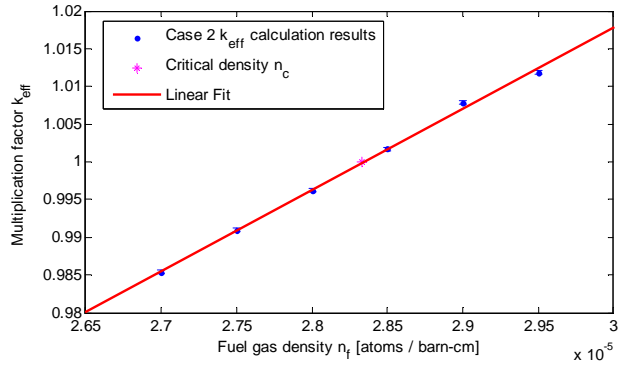
(b) Case 2
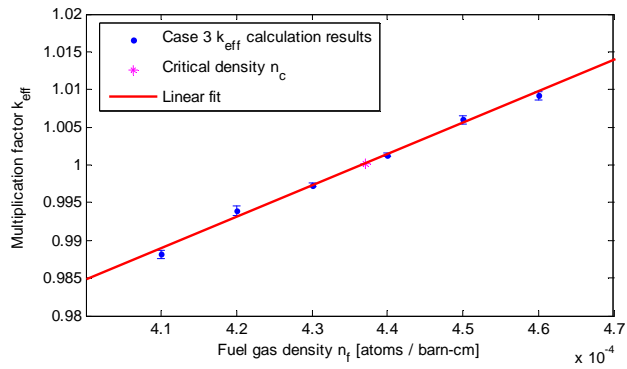
(c) Case 3

Figure 2.3: Multiplication factor k_{eff} as a function of the fuel gas density n_f for the three core cases. Included are error bars showing the standard deviations from the MCNP k_{eff} calculations. The linear fits were used to evaluate the critical density n_c and normalized reactivity coefficient of the fuel α'_n.
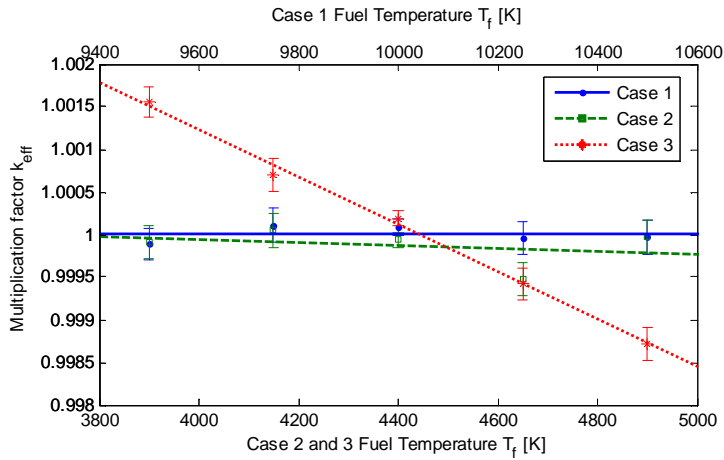
Figure 2.4: Plots of the multiplication factor k_{eff} as a function of fuel temperature T_f for the three core cases. The error bars show the standard deviation for the k_{eff} calculations. The resulting linear fits are shown as straight lines, their gradient representing the reactivity coefficient of the fuel temperature α_{Tf}.

2.3.5 Fuel Temperature Reactivity Coefficient

In most reactors one of the main stabilizing factors is the fuel temperature feedback on the reactivity. The reactivity coefficient of the fuel temperature, $\alpha_{Tf} = \frac{\partial k}{\partial T_f}$, was calculated for the three GCR cases. Criticality calculations were performed with the fuel temperature T_f perturbed by 250 K and 500 K respectively, and on the data points a linear fit was made. Plots of the calculated k_{eff} versus T_f and the linear fits are in figure 2.4. Calculated reactivity coefficient of the fuel temperature for all three cases are given in table 2.5 in pcm (10^{-5}) per Kelvin.

In van Dam and Hoogenboom reactivity coefficients for the fuel temperature were not calculated, but it was mentioned the nuclear Doppler effect of the fuel will be enough to compensate for small reactivity changes ($\sim$ 100 pcm). As can be seen from table 2.5 this is not the case for cases 1 and 2 with high enriched fuel. For these cases α_{Tf} is in the order of -0.01 pcm/K or smaller, as was also mentioned in other research [Dugan,1989]. For the high enriched cores, the uranium density is very low, and the neutron mean-free-path length of absorption for non-thermal neutrons is so large (> 100 m), neutrons have almost negligible chance of being captured in resonances before being moderated in the reflector. Because of this a widening of the resonances due to a rise of fuel temperature will have almost no effect on the criticality. For case 3, with low enriched fuel, the uranium density is much higher, over 10 times, and the ^{238}U density, which has the largest resonances, is more then 20 times higher. As a result, the mean-free-path length for absorption of non-thermal neutrons is no longer extremely large compared to the core radius, and there is significant absorption of neutrons in the resonances. Thus α_{Tf} for case 3 is much larger than for case 1 and 2 and might be an important factor for reactor control.

21

Table 2.5: Reactivity coeffients of the fuel temperature α_{Tf} at criticality for the three core cases in pcm/K (10^{-5}/K). Also given is the fuel temperature T_f at criticality. α_{Tf} for case 1 and 2 was too small to evaluate.

	T_f [K]	α_{Tf} [pcm/K]
Case 1	10000	$\|\alpha_{Tf}\| \leq 0.01$
Case 2	4400	$\|\alpha_{Tf}\| \leq 0.01$
Case 3	4400	-0.3

2.3.6 Reflector Temperature Reactivity Coefficient

Another important reactivity coefficient for reactor stability is the reactivity coefficient of the reflector (moderator) temperature $\alpha_{Tr} = \frac{\partial k}{\partial T_r}$. As mentioned before an increase in the reflector temperature T_r will result in a hardening of the thermal neutron spectrum, which will lower the absorption probability of neutrons in the fuel. The absorption of neutrons in the graphite however also lowers with increased neutron energy, thus lowering the probability of neutrons being absorbed in the reflector. The first effect is usually more important than the second one, and thus an increase in reflector temperature results in a lower reactivity. The effect of changes of the reflector temperature on the reactivity was calculated for the three GCR core cases.

The graphite reflector was represented in MCNP using thermal $S(\alpha, \beta)$ cross-section libraries for solid graphite. These data sets include the effects of the graphite bonds in solid graphite on the cross sections, which are not included in the normal free-gas treatment of nuclides by MCNP. For the graphite reflector, the free-gas treatment is used down to the neutron energy where $S(\alpha, \beta)$ data is available, typically below 4 eV. At that point, the $S(\alpha, \beta)$ data automatically overrides the free-gas treatment. In general, $S(\alpha, \beta)$ effects are most significant for neutron energies below 2 eV. Since in a GCR the neutron flux is mostly thermal, especially inside the reflector (see appendix C), the $S(\alpha, \beta)$ data set is much more important for the neutron behaviour inside the reflector than the free-gas treatment. In MCNP thermal $S(\alpha, \beta)$ cross-section libraries are only available for certain temperature values, while the free-gas treatment can deal with any user-defined temperature. Since the free-gas treatment is of only minor importance inside the reflector, calculations were performed only for reflector temperatures for which $S(\alpha, \beta)$ data was available.

Plots of the MCNP criticality calculations for the different reflector temperatures for each of the three cases are given in figure 2.5. From these plots α_{Tr} was evaluated by a linear fit around the critical reflector temperature ($T_r = 1000$ K for case 1, and $T_r = 1900$ K for case 2 and 3). The calculated α_{Tr} are given in table 2.6 for all three cases.

For case 1 $\alpha_{Tr} = -7.9$ pcm/K, which is comparable with $\alpha_{Tr} = -9$ pcm/K given in van Dam and Hoogenboom for a spherical GCR with otherwise identical properties. Since that α_{Tr} was evaluated using a parametric relation between the fuel gas density n_c, reflector temperature T_r and core radius R_c, the value from van Dam and Hoogenboom can be considered to have a large uncertainty, and thus not be significantly different from the calculated value of $\alpha_{Tr} = -7.9$ pcm/K.

Table 2.6: Reactivity coefficients of the reflector temperature α_{Tr} near criticality for the three GCR core cases in pcm/K (10^{-5}/K). Also given is the reflector temperature T_r at criticality.

	T_r [K]	α_{Tr} [pcm/K]
Case 1	1000	-7.9
Case 2	1900	-6.7
Case 3	1900	-3.9

As mentioned before, case 2 has a larger l_a/R_c value than case 1, thus neutrons will enter the reflector more often before being absorbed in the fuel. Because of this, the positive reactivity effect of lowering the absorption in the reflector with increasing T_r is more important in case 2 than in case 1. This results in a slightly lower α_{Tr} for case 2. For case 3 α_{Tr} is significantly lower than for case 1 and 2. Main reason is the higher absorption of thermal neutrons in ^{238}U due to the larger ^{238}U density. Lowering the reflector temperature will increase the absorption in the fuel by ^{235}U, but also the absorption by ^{238}U. Since the ^{238}U density is much larger in case 3, this increase in absorption in ^{238}U has a significant effect on the reactivity, resulting in a lower increase in reactivity.

In case 3, it can be seen in figure 2.5 that α_{Tr} changes sign at reflector temperatures below 600 K. The cause of this might be the much higher ^{238}U density. The ^{235}U(n, f) cross section has a small fluctuation around 10^{-7} eV, which means a shift in the neutron energy peak in this region could result in a smaller change on the absorption in ^{235}U, resulting in a lower α_{Tr}. This can be observed in the data for cases 1 and 2 at $T_r < 600$ K. In case 3 however, this would cause the change in the absorption in ^{238}U to become dominant in this T_r region, resulting in a positive α_{Tr}. Since this change of sign is at reflector temperatures well below normal operating temperatures of a GCR, this will not have any major effects on the reactor control.

In general, the reactivity coefficients of the reflector temperature show a strong negative feedback. This is an important safety mechanism in case of an accident resulting in a loss of coolant of the reflector. A rise in reflector temperature of even a few hundred K will result in a significant reduction in reactivity, resulting in a shutting down of the fission chain reaction. For control purposes of the core temperature, α_{Tr} is less suitable, due to the delay between a rise of power and a rise in reflector temperature, because of the large reflector bulk.

2.4 Conclusions

In the previous sections several properties of the neutronics of a gas core reactor were calculated using MCNP and evaluated for three different core setups. All calculated values for the reference case, case 1, were in accordance with values found in literature, giving us confidence in the validity of the results for the other core cases.

The slightly higher specific power density near the core wall might indicate a change in the fuel density distribution towards a distribution with higher den-
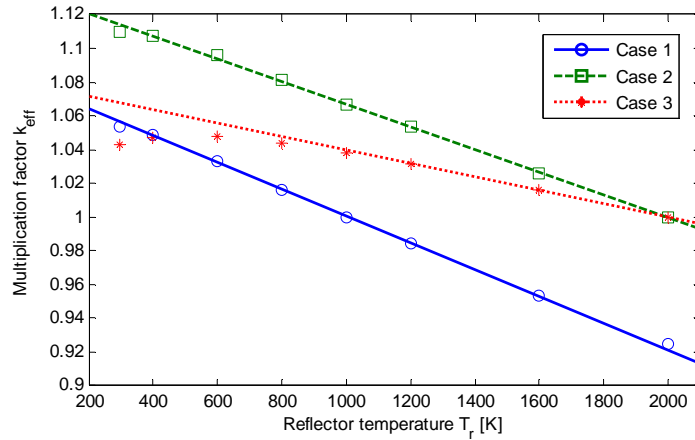
Figure 2.5: Plots of the multiplication factor k_{eff} as a function of the reflector temperature T_r for the three core cases. The resulting linear fits are shown as straight lines, their gradient represents the reactivity coefficient of the reflector temperature α_{Tr}.

sities near the wall will lead to an increase in fission, and thus an increase in reactivity. Although the densities inside a GCR are low, and even doubling or tripling the density near the wall would still result in mean-free-path lengths in the order of meters in that zone, the differences in $f(r)$ itself are also small. Thus, due to increased absorption and scattering near the wall, such a fuel redistribution could possibly effect $f(r)$ enough to negate the positive effect of redistributing fuel towards that region. An effort was made to calculate the reactivity coefficient of the fuel for each radial zone inside the core. Unfortunately, the statistical nature of MCNP did not permit to calculate such small perturbations with sufficient precision to draw any conclusions. The effect of fuel redistribution on the neutronics is further investigated in chapter 4.

Comparing the various feedbacks a possible source of instabilities of the GCR cores can be identified. The reactivity coefficient of the fuel α'_n is such, that a change in pressure of a few percent could insert 1\$ of reactivity in the core. The low enriched core has a lower reactivity coefficient of the fuel, but still pressure changes of a few percent would result in making the reactor prompt critical. These pressure changes can easily occur due to numerous malfunctions, for example a blockage upstream of the core exit, or a malfunction in the fuel pump. The instantaneous reactivity feedback of the fuel temperature is for the high enriched cores almost absent. For low enriched cores, the reactivity coefficient of the fuel is still insufficient to counter such a reactivity insertion, as this would require fuel temperature changes in the thousands of Kelvin.

Reactor control also depends on delayed feedbacks of the reflector temperature, and of the fuel density through a pressure change due to a change in fuel gas temperature. The bulk of the graphite is quite large, thus the time scale of this feedback would be insufficient to counter a sudden reactivity insertion. The time scale of a pressure change resulting in a lower density depends on the speed of sound in the fuel gas, and on the reactor size. Typical core sizes

are in the order of 3 m [Anghaie,2005], and the speed of sound inside a GCR is $\sim$ 1000 m/s [Dugan,1993], resulting in a time scale of 0.003 seconds. The neutron prompt removal life time of the GCR was calculated by MCNP to be the same, 0.003 s. Thus a complicated system of feedbacks on the reactivity exists, with an instant fuel temperature feedback, a delayed but fast feedback through the density change due to a temperature and pressure change, and a delayed feedback from the reflector temperature, all with comparable orders of magnitude for case 3. Whether these feedbacks have a stabilizing effect on the reactor or result in power fluctuations growing out of control will depend on their respective values and time-scales. Thus a detailed, time-dependent model of the flow-field inside a GCR and of the heat transfer would be needed to evaluate the stability of a GCR.

Several other GCR designs based on oscillating systems subvert this problem, and even depend on the large reactivity coefficient of the fuel and the delay on the reactivity feedback through a change in fuel pressure due to a rise of fuel temperature [Panicker,1990, Kuijper,1992].

Chapter 3

Heat Transfer Model

The subject of this chapter is the development of a model describing the heat transfer inside the core of a gas core reactor, and the calculation of the radial temperature and density profiles inside the GCR model. The fuel gas consists of a gas mixture of uranium- and carbon-fluorides, in thermochemical equilibrium with the inner wall of the graphite reflector. As in chapter 2, a one-dimensional model of an infinite cylinder is used for the core, with no axial or tangential dependencies. For this model, a computational tool is developed to calculate the radial temperature and fuel density distribution inside the core. In a GCR core, due to the high temperatures, the large molecules forming the UCF gas fall apart into multiple smaller molecules, a process called dissociation. This dissociation effect is included in the heat transfer model, as well as the effects of radiative and kinetic (diffusive) heat transfer.

In the first section the core model and its simplifications are explained. Next the heat transfer equation is derived. In the third section the thermophysical properties of the UCF gas needed to solve the heat transfer equation are evaluated. Section 3.4 details the numerical solution method used to solve the heat transfer equation, followed by a section describing the distribution of the volume cell grid on which the heat transfer equation was solved. Several tests on the consistency of the developed code are detailed in the next section. In section 3.7 the code was validated by comparing calculations with the code against calculations done by van Dam and Hoogenboom [1983]. The next section contains results of heat transfer calculations on the three core cases described in the previous chapter, giving the temperature and density distribution for a given average fuel temperature, as well as the pressure inside the core and the thermal power generated inside the core to sustain these temperatures. The last section contains conclusions drawn on the important parameters for the heat transfer inside a GCR.

3.1 Model Assumptions

For the heat transfer model, the same geometric core model as in figure 2.1 is used consisting of a cylindrical cavity filled with UCF gas, surrounded by a graphite reflector. Axial and tangential dependence is ignored, resulting in a one-dimensional model, with only radial dependence.

It is assumed the atomic ratios of fuel mixture stay the same throughout the entire reactor. In reality, dissociation of the fuel gas will cause a mixture of many different elements to exist inside the core. The concentration differences of these mixtures will cause transport of the various elements to regions with different dissociation levels, resulting in local changes in the atomic ratios of the fuel mixture. Calculation of the actual atomic ratios at every location in the fuel gas is not possible without making a model including concentrations and reaction rates of all the different molecules in the dissociating gas mixture inside a GCR, which is beyond the scope of this research. Since resulting changes in the fuel mixture will cause concentration differences in the opposite direction, the error made in this assumption is expected to be small.

There is also assumed to be no fuel flow through the cylinder and the pressure is assumed uniform, so the fuel is considered to be stationary. This significantly simplifies the calculations, since there will only be diffusive elements in the transport equations (no convective transport). Including axial flow or radial pressure gradients (needed for both transient calculations and a more realistic steady state operational core model with axial fuel flow) was expected to be too much work to fit inside the timescale of this project. This decision means only steady state solutions can be calculated.

Although the resulting temperature and density profiles will not give a realistic description of a GCR core during operation, approximate guesses for the temperature and density profiles in an operating GCR core can still be investigated, as well as the effect of fuel dissociation on these profiles. Also the model will help to gain a fundamental understanding of the heat transfer in a GCR.

3.2 The Heat Transfer Equation

The heat transfer equation, in the absence of flow, dissipation due to internal friction and pressure gradients, can be written as [Rohsenow,1973]

$$\rho c_p \frac{\partial T}{\partial t} = Q + \nabla \cdot \lambda \nabla T - \nabla \cdot \vec{q}_r \tag{3.1}$$

where ρ is the density of the medium, c_p is the heat capacity, T is the temperature, λ is the thermal conductivity, Q is the heat production or power density, and $\vec{q}_r$ is the radiative heat flux.

The radiative heat transfer was modelled using the Rosseland diffusion approximation [Modest,1993]. It is valid when the mean-free-path of photons is small compared to the geometry. In this model, the radiative heat flux $\vec{q}_r$ is described as a result from the diffusion of the radiation density u according to

$$\vec{q}_r = -D_r \nabla u \tag{3.2}$$

with the radiative density u given by

$$u = \frac{4}{c} \sigma_{SB} T^4 \tag{3.3}$$

with c the speed of light and σ_{SB} the Stefan-Boltzman constant. The radiative diffusion coefficient D_r can be written as

$$D_r = \tfrac{1}{3} c l_{ph} \tag{3.4}$$

with l_{ph} the photon mean-free-path, which can be calculated by

$$l_{ph} = \frac{1}{n\sigma_{ph}} \qquad (3.5)$$

where n is the molecular density of the gas and σ_{ph} is the microscopic photon collision cross section. By combining equations 3.2 to 3.5 the radiative heat flux can be written as a diffusion effect

$$\vec{q_r} = -\frac{1}{3}\frac{c}{n\sigma_{ph}}\nabla\frac{4}{c}\sigma_{SB}T^4 = -\frac{16}{3}\frac{\sigma_{SB}}{n\sigma_{ph}}T^3\nabla T = -\lambda_r\nabla T \qquad (3.6)$$

with λ_r the radiative thermal conductivity given by

$$\lambda_r = \frac{16}{3}\frac{\sigma_{SB}}{n\sigma_{ph}}T^3 \qquad (3.7)$$

In the rest of this thesis, the thermal conductivity of the UCF gas, λ in equation 3.1, will be called the kinetic thermal conductivity λ_{kin}, as in Klein [1987], to distinguish it from the radiative thermal conductivity, and is described in paragraph 3.3.3. The kinetic thermal conductivity can be combined with the radiative thermal conductivity into a total thermal conductivity λ_{tot} as

$$\lambda_{tot} = \lambda_r + \lambda_{kin} \qquad (3.8)$$

The particle density of the fuel gas n is assumed to follow the ideal gas law, and is calculated by

$$n = \frac{p}{kT} \qquad (3.9)$$

with k the Boltzmann constant and p the pressure in the reactor core. n and T are functions of the position inside the core. As the ideal gas law must hold at every location, the pressure, which is constant throughout the core, must satisfy the ideal gas law at every location. As explained in section 3.3.1, the dissociation function $g(p, T)$ is defined as the relation between the original number of molecules N_0 and the actual number of molecules N. By dividing by volume, the dissociation function can be written as

$$g = \frac{n}{n_0} \qquad (3.10)$$

with n_0 the local molecular density in the case there would be no dissociation. The total number of original molecules N_0 in the system must be equal to

$$N_0 = \int_V n_0 dV = \int_V \frac{p}{kTg}dV = \frac{p}{k}\int_V \frac{1}{Tg}dV \qquad (3.11)$$

where we have used equations 3.9 and 3.10. This can be rearranged to get an expression for the pressure

$$p = \frac{N_0 k}{\int_V \frac{1}{Tg}dV} \qquad (3.12)$$

given an initial number of undissociated molecules N_0 in the system.

In our GCR model the power density Q is only due to fission and is described by

$$Q = f\rho_U \qquad (3.13)$$

where f is the specific power density as defined in equation 2.7, and ρ_U is the uranium density inside the core. The total thermal power P generated inside the core is given by

$$P = \int_V Q dV = \int_V f \rho_U dV \qquad (3.14)$$

and the specific power f was scaled such that equation 3.14 was satisfied.

ρ_U can be calculated from the particle density n, using the assumption the atom ratios of the fuel mixture stay equal throughout the entire reactor

$$\rho_U = n_U m_U = n_0 \frac{f_U}{f_U + f_C} m_U = \frac{n}{g} \frac{f_U}{f_U + f_C} m_U \qquad (3.15)$$

with n_U the uranium atom density, m_U the atomic mass of uranium, depending on enrichment, and $\frac{f_U}{f_U + f_C}$ is the number of uranium atoms per undissociated molecule in the fuel mixture.

Combining equations 3.1, 3.6, 3.8 and 3.13 results in the following form of the heat transfer equation

$$\rho c_p \frac{\partial T}{\partial t} = f \rho_U + \nabla \cdot \lambda_{tot} \nabla T \qquad (3.16)$$

which is used to describe the heat transfer in the fuel gas in our heat transfer code.

Equation 3.16 was solved with boundary conditions of

$$r = 0 \quad \rightarrow \quad \nabla T = 0 \qquad (3.17)$$

$$r = R_c \quad \rightarrow \quad T = T_{wall} \qquad (3.18)$$

where $r = 0$ is at the centre of the core, and $r = R_c$ at the interface with the graphite reflector, with $T_{wall} = 2000$ K the inner wall temperature of the graphite reflector.

The temperature profile in the graphite reflector was calculated at steady state, using the following form of the heat transfer equation

$$\vec{q} = \lambda_{graph} \nabla T \qquad (3.19)$$

with λ_{graph} the thermal conductivity of the graphite reflector, and $\vec{q}$ the heat flux through the graphite reflector. Boundary conditions were an inner wall temperature of $T = T_{wall}$ at $r = R_c$ and a heat flux of $\vec{q} \cdot \hat{n} = \frac{P}{A}$ with A the total area of the graphite cylinder perpendicular to the heat flux.

3.3 Thermophysical Properties of the UCF Gas

The fuel in the GCR core model consisted of a mixture of UF_4, UF_5 and CF_4 molecules, with atom ratios for U:C:F of 0.70 : 0.18 : 4.00. This mixture is, at 2000 K and 25 bar, in chemical equilibrium with a graphite wall; the reflector. Different wall temperatures or gas pressures will cause corrosion or deposition of carbon at the reflector wall.

At high temperatures (starting at ~ 2500 K), the larger fluoride molecules fall apart and dissociate into smaller molecules, creating a mixture of $U_m F_n$, $C_m F_n$, U, C and F_n particles. At even higher temperatures, starting around

6000 K, the atoms start to ionize, resulting in 5-10% (depending on pressure) of the particles being ionized at 10000 K [Klein,1991a]. At higher pressures dissociation and ionization start at higher temperatures. The various (thermo) physical properties of the UCF gas mixture at temperatures of 2000 - 10000 K and pressures of 1 - 100 bar were investigated by Boersma-Klein and Kistemaker [Klein,1987, Klein,1989, Klein,1991a, Klein,1991b]. The results of their research were used to evaluate the different properties of the UCF gas in our model. In the next paragraphs the modelling of these properties is detailed.

3.3.1 Dissociation Function

As mentioned above, the large molecules of the UCF gas mixture dissociate at higher temperatures into smaller molecules. A dissociation function $g(p,T)$ can be defined as the relation between the original number of molecules N_0, at reference pressure $p_0 = 1$ bar and temperature $T_0 = 2000$ K, and the number of molecules at the current pressure and temperature $N(p,T)$.

$$g(p,T) = \frac{N(p,T)}{N_0} \tag{3.20}$$

Assuming all seperate molecules still follow the ideal gas law

$$pV = NRT \tag{3.21}$$

where R is the universal gas constant and V is the volume, we can combine equation 3.21 with equation 3.20 to find a relation for g as a function of temperature and pressure.

$$pV = N(p,T)RT = gN_0RT \rightarrow \tag{3.22}$$

$$g(p,T) = \frac{pV}{N_0RT} \tag{3.23}$$

In Klein [1991a] a numerical equation of state is derived for the UCF gas mixture, giving a relation between its pressure, temperature and volume. The relationship between the pressure and the volume of an initial amount of $N_0 = 0.876$ moles of UCF gas is given as

$$p_{bar}V_l^{-a} = 10^b \tag{3.24}$$

for the pressure p_{bar} in bar and the volume V_l in liters. a and b are functions of T. After rewriting 3.24 to

$$V = V_l \cdot 10^{-3} = p_{bar}^{\frac{1}{a}} \cdot 10^{-\frac{b}{a}} \cdot 10^{-3} \tag{3.25}$$

we can substitute V in equation 3.23 to get

$$g(p,T) = \frac{p \cdot p_{bar}^{\frac{1}{a}} \cdot 10^{-\frac{b}{a}} \cdot 10^{-3}}{0.876 \cdot R \cdot T} \tag{3.26}$$

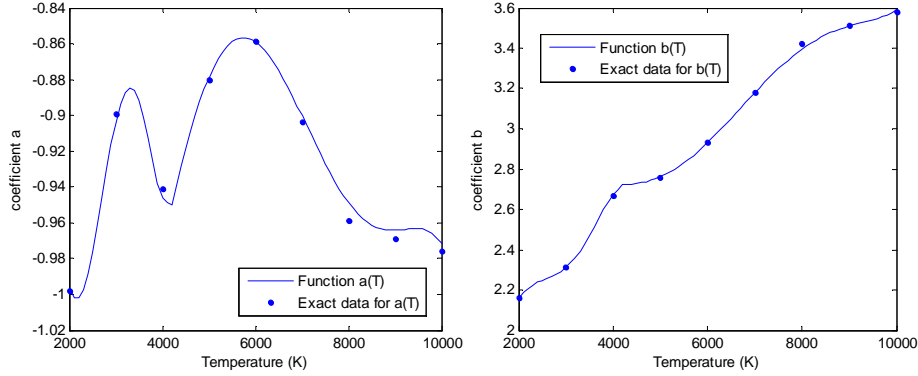an equation for the dissociation function g as a function of p and T. For $a(T)$

Figure 3.1: Plots of the coefficients $a(T)$ and $b(T)$ using equations 3.27 - 3.30. The dots are data points given in Klein.

and $b(T)$, the following equations were given

For $2000 < T < 4200$

$$a(T) = -3.576 + 6.69339 \cdot T' - 6.452637 \cdot T'^2$$
$$+ 2.801388 \cdot T'^3 - 0.5611048 \cdot T'^4 + 0.042220499 \cdot T'^5 \qquad (3.27)$$

$$b(T) = 0.0287 + 0.4469 \cdot T' + 1.925646 \cdot T'^2$$
$$- 1.3965195 \cdot T'^3 + 0.35629045 \cdot T'^4 - 0.03104086 \cdot T'^5 \qquad (3.28)$$

For $4200 < T < 10000$

$$a(T) = 2.1393 - 3.19189 \cdot T' + 1.169843 \cdot T'^2$$
$$- 0.19514 \cdot T'^3 + 0.0151843 \cdot T'^4 - 4.48793 \times 10^{-4} \cdot T'^5 \qquad (3.29)$$

$$b(T) = -3.17545 + 5.66073 \cdot T' - 2.067737 \cdot T'^2$$
$$+ 0.3552273 \cdot T'^3 - 0.02841493 \cdot T'^4 + 8.58538 \times 10^{-4} \cdot T'^5 \qquad (3.30)$$

with $T' = T \times 10^{-3}$. See figure 3.1 for plots of $a(T)$ and $b(T)$ versus the UCF-gas temperature.

In figure 3.2 the dissociation function g is plotted for various pressures in the temperature range 2000-10000 K. The dots are data points from table 3 in Klein [1991a], the lines are plotted using function 3.26 and values of a and b from equations 3.27 - 3.30. As can be seen, the functions for $a(T)$, and $g(p, T)$ sometimes deviate from the exact data. When comparing the function for $a(T)$ with a plot in Klein, it was concluded a mistake was made in the function given for $a(T)$. Unfortunately, not enough data points were available to fit a new function for $a(T)$ to.

3.3.2 Density

For most gases, the density at constant pressure scales with the inverse of the temperature T, according to the ideal gas law. In the GCR core however, the UCF gas will dissociate at higher temperatures and the large molecules will fall apart into multiple smaller, lighter molecules. The particle density n will still follow the ideal gas law, see equation 3.9, but the gas density ρ will decrease
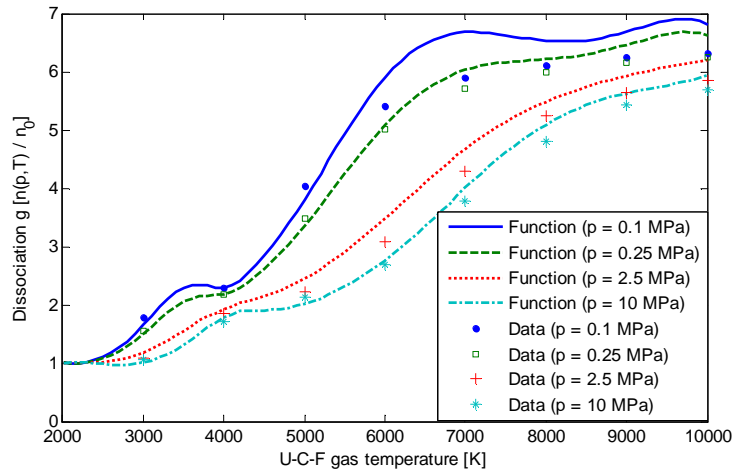
31

Figure 3.2: Dissociation function $g(p,T)$ for various pressures as a function of temperature. The dots are data points from Klein [1991a]. The continuous lines are plotted using equation 3.26.

proportionally to the level of dissociation. Since we assume the atomic ratios of the fuel gas do not change, the density ρ can be calculated using equations 3.9 and 3.10 by

$$\rho\left(p,T\right) = n_0 W = \frac{p}{kT}\frac{W_0}{g} \tag{3.31}$$

with W_0 the average weight per molecule of the original, undissociated mixture.

Since g becomes larger at higher temperature and lower pressure, the density will no longer scale linear with pressure or inversely linear with temperature, but will react more extremely. See figure 3.3 for a plot of the UCF gas density ρ for pressures of 1 and 100 bar, together with the particle density n, which follows the ideal gas law.

3.3.3 Kinetic Thermal Conductivity

The 'regular' or kinetic thermal conductivity λ_{kin} is normally only due to diffusion. But in the case of a dissociating mixture, temperature gradients will cause concentration gradients of the different components of the mixture, which in turn will cause diffusion of the seperate components. To account for these effects, the effective kinetic thermal conductivity λ_{kin} is composed of three parts

$$\lambda_{kin} = \lambda_{tr} + \lambda_{int} + \lambda_{react} \tag{3.32}$$

in which λ_{tr} is the translational thermal conductivity and represents the kinetic energy flux, λ_{int} is the internal thermal conductivity, and λ_{react} is the reactant thermal conductivity [Klein,1991b]. The last term is due to concentration gradients arising from different dissociation levels due to a temperature gradient. This will induce the movement of dissociated molecules from high temperatures towards regions of lower temperatures, where they recombine (and the other way around). The recombination and dissociation reactions deposit or extract
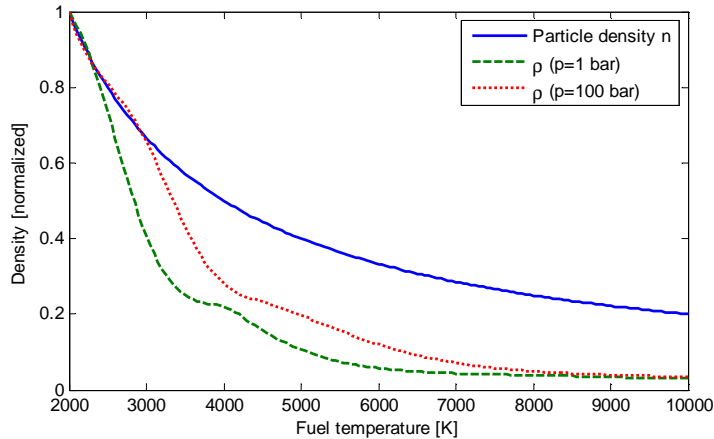
Figure 3.3: UCF gas density ρ as a function of temperature for a pressure of 1 and 100 bar. Also given is the particle density n, following the ideal gas law. Functions are normalized to a density of 1 at $T = 2000$ K.

a relatively large amount of energy to or from the gas, resulting in large values for λ_{kin} at p, T values at which the dissociation function g has a large gradient. At these p, T values small changes in T will result in large changes in the chemical composition of the gas, and in relatively large concentration gradients. See figure 3.4.

Values for λ_{kin} were evaluated for a continuous pressure interval from 1-100 bar from the two plots in figure 3.4 of λ_{kin} at pressures of 0.1 and 10 MPa, reproduced from Klein. First, data points were evaluated from the figures, and λ_{kin} values could be evaluated for pressures of 0.1 and 10 MPa between 2000 and 6000 K, using linear interpolation between these points. For $p = 0.1$ MPa λ_{kin} was extrapolated to a value of 1800 K, assuming λ_{react} would go to zero and λ_{int} and λ_{tr} would stay the same. For temperatures above 6000 K, and for $p = 10$ MPa for $T < 2000$ K, the thermal conductivity of 6000 K or 2000 K was used.

To calculate values of λ_{kin} at pressures between 0.1 and 10 MPa, the values could not be directly interpolated using $\lambda_{kin}(p = 0.1, T)$ and $\lambda_{kin}(p = 10, T)$. This would not take into account the shift in the maxima and minima with changing pressures. When comparing the figures for $p = 0.1$ and $p = 10$ MPa, the figure for $\lambda_{kin,10}$ looks like $\lambda_{kin,0.1}$, but shifted over temperature, stretched out a bit, and with lower peaks. In other words, with rising pressure the graph for λ_{kin} is shifted and stretched, and the maximum values are lowered. To account for these effects, a relationship between the graphs of $\lambda_{kin,0.1}$ and $\lambda_{kin,10}$ was sought by assuming that a point $T_{0.1}$ on the graph for $p = 0.1$ MPa corresponds to a point $T_{10} = A + BT_{0.1}$ on the graph for $p = 10$ MPa. By looking at the location of the maxima and minima of the graphs, the following relationship was found.

$$T_{10} = (T_{0.1} - 1500)\frac{22}{13} + 1500 \qquad (3.33)$$

It was assumed that the temperature for which we wanted to evaluate λ_{kin} should lie on a line between these two temperatures, interpolating based on the
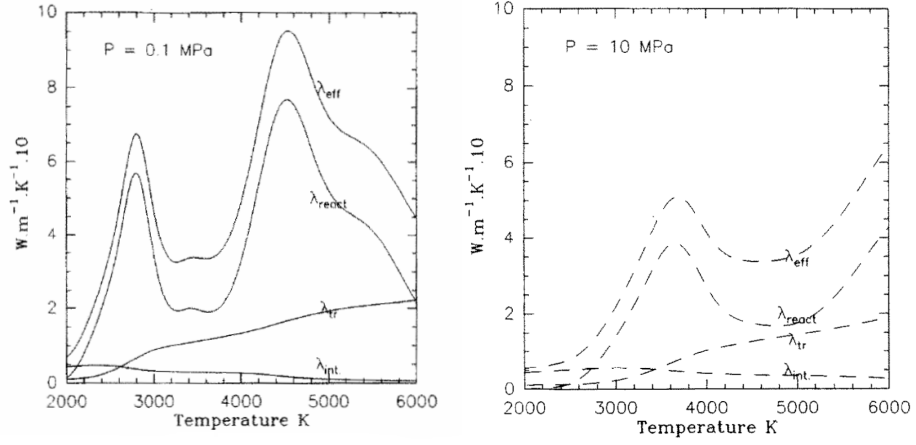
Figure 3.4: Kinetic thermal conductivty components at $p = 0.1$ MPa and $p = 10$ MPa from Klein. λ_{eff} is the total kinetic thermal conductivity λ_{kin}.

pressure. In other words, the temperature we are interested in, T, must lie in between $T_{0.1}$ and T_{10}, with linear interpolation on $\log(p)$

$$T = aT_{0.1} + (1 - a)T_{10} \tag{3.34}$$

$$a = \frac{1}{2} - \frac{1}{2}\log(p) \tag{3.35}$$

with p in MPa. Using 3.33 to eliminate either $T_{0.1}$ or T_{10} from 3.34, equations were found for the temperature corresponding to T on the graphs for $p = 0.1$ and $p = 10$ MPa

$$T_{0.1} = \frac{13T + 13500(1 - a)}{22 - 9a} \tag{3.36}$$

$$T_{10} = \frac{22T - 13500a}{22 - 9a} \tag{3.37}$$

and the thermal conductivity for an arbitrary temperature T and pressure p could be calculated by

$$\lambda_{kin}(p, T) = a\lambda_{0.1}(T_{0.1}) + (1 - a)\lambda_{10}(T_{10}) \tag{3.38}$$

where $\lambda_{0.1}$ and $\lambda_{0.1}$ are the thermal conductivities at $p = 0.1$ and 10 MPa.

The thermal conductivity, calculated using the method described above, is plotted for various pressures in figure 3.5.

3.3.4 Heat Capacity

To be able to evaluate the heat capacity $c_p(p, T)$ of the UCF gas mixture for all pressures between 0.1 and 10 MPa and temperatures from 2000 to 10000 K, the same method was used as for the thermal conductivity. From plots of $c_p(p, T)$ for p = 0.1, 2.5 and 10 MPa [Klein,1991a] points were evaluated and functions for c_p could be constructed using linear interpolation (see Figures 3.6, 3.7 and 3.8).
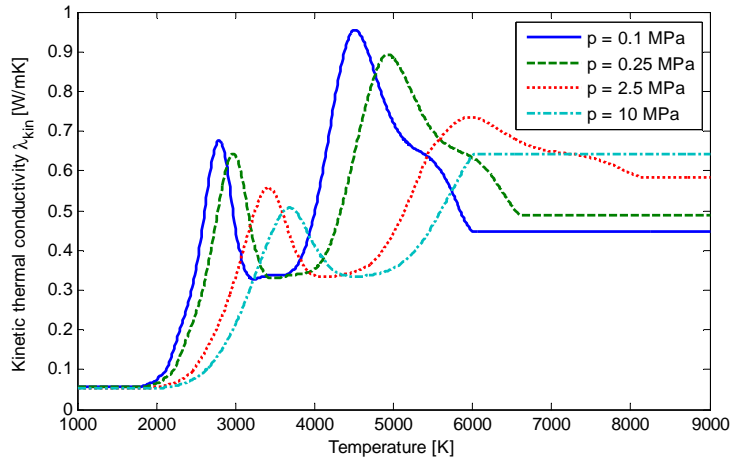
Figure 3.5: Kinetic thermal conductivity λ_{kin}, calculated for pressures of 0.1, 1, 2.5 and 10 MPa.
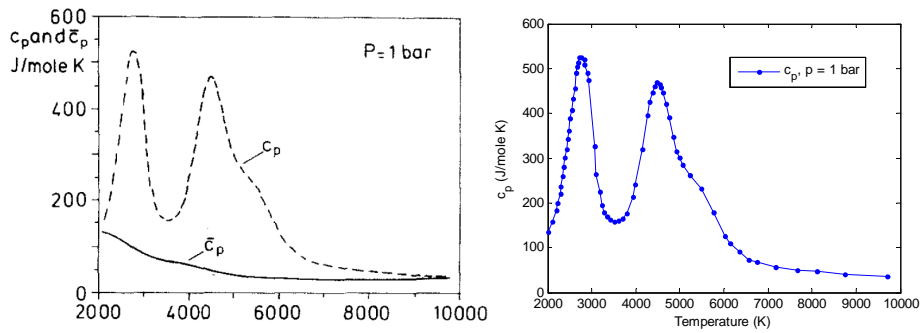

Figure 3.6: Heat capacity of the UCF fuel gas at a pressure of 0.1 MPa from Klein, with right the evaluated data points and linear interpolated function.
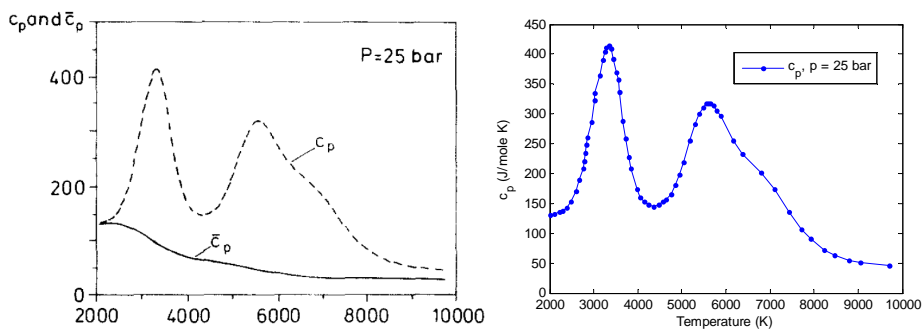

Figure 3.7: Heat capacity of the UCF fuel gas at a pressure of 2.5 MPa from Klein, with right the evaluated data points and linear interpolated function.
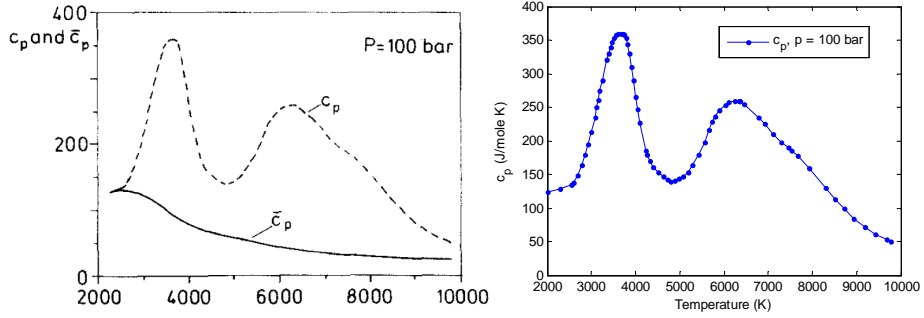
Figure 3.8: Heat capacity of the UCF fuel gas at a pressure of 10 MPa from Klein, with right the evaluated data points and linear interpolated function.
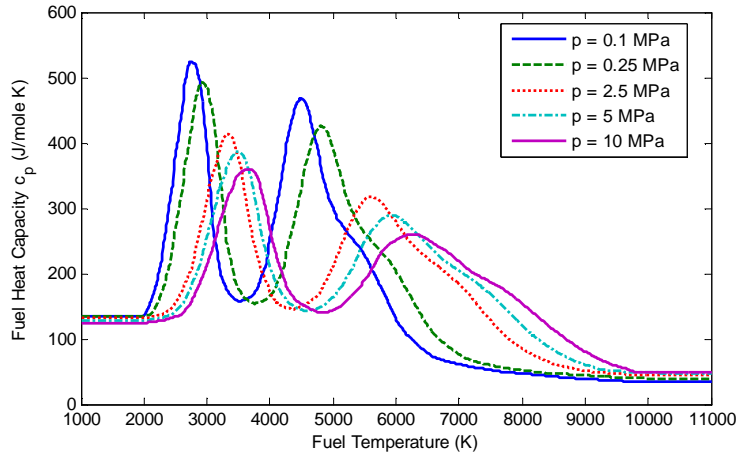

Figure 3.9: Heat capacity c_p of the UCF fuel gas evaluated at different pressures, using interpolation based on the shifting and stretching of the functions with rising pressure.

As with the thermal conductivity, an interpolation scheme based on the shifting and stretching of the peaks and the local minimum was used. At temperatures above 10000 K or below 2000 K, the c_p value at 10000 K or 2000 K was used. Results of c_p evaluated at various pressures using this method are plotted in figure 3.9.

Since the heat transfer equation, equation 3.16, is only solved for steady state, $c_p(p, T)$ is not used. At the start of this project it was not clear only steady state solution would be sought during this research, thus values for $c_p(p, T)$ were evaluated and included in the code. The results are given here for future use, as they are needed for time-dependent calculations, such as transients.

3.3.5 Photon Cross Section and Mean-Free-Path

In the Rosseland diffusion approximation, the radiative thermal conductivity λ_r depends on σ_{ph}, the microscopic photon cross section, a property of the gas, see

36

equation 3.7. For different molecules, even consisting of the same atoms, this cross section can differ strongly. Few data is available on photon cross sections for UF_n gases, especially at high temperatures. Data for a few of the components (UF_4, U and F) of the UCF gas mixture was available from Watanabe [1993], which also showed some temperature dependence of the various cross sections. In van Dam [1983] and Kuijper [1992] a constant photon cross section per molecule for the UCF gas mixture of $\sigma_{ph} = 2.5 \times 10^{-21}$ m^2 was used. Given the many unknowns, the value used in previous work on the UCF gas mixture of $\sigma_{ph} = 2.5 \times 10^{-21}$ m^2 was used, with the sidenote that it might differ for certain p, T values by as much as a factor 10.

The Rosseland diffusion model for radiative heat transfer is valid when the photon mean-free-path length is much smaller than the geometry, and when more than a photon mean-free-path away from a wall. Using case 1 from table 2.1 as a reference, the UCF gas density was $n_c = 3.18 \times 10^{-5}$ atoms/barn-cm. With a gas mixture consisting of 70% UF_4 and 30% CF_4, this translates to 6.31×10^{24} molecules/m^3 (without dissociation), resulting in a photon mean-free-path length l_{ph} of

$$l_{ph} = \frac{1}{n\sigma_{ph}} = \frac{1}{6.31 \times 10^{24} \cdot 2.5 \times 10^{-21}} = 6.3 \times 10^{-5} \, \text{m} \qquad (3.39)$$

multiple orders smaller than the radius of the cylinder of 1.18 m, and even smaller than the smallest volume cell used in our numerical solver. For calculations with a lower enrichment, the critical density of the gas is even higher, and the mean-free-path length is lower. Thus it was concluded the Rosseland model for radiative heat transfer is valid for all our calculations.

3.4 Numerical Solution Method

To calculate the temperature distribution inside a GCR, the heat transfer equation derived in section 3.2, equation 3.16, was discretized using a finite volume method over a non-uniform grid. The resulting linear system was solved using a linear solver. Since the solver calculated the temperature profile, but most of the physical properties also depend on temperature, the temperature distribution was solved in several iterations, each time using the most recent temperature field to evaluate the physical properties inside the system.

Discretization

The one-dimensional geometry was discretized over non-uniform volume cells with cell with Δr_i for cell i, width $i = 1$ the index of the cell closest to the centre of the core. The distribution of the volume cell widths is detail in section 3.5. The location of the cell centres and borders are indicated in figure 3.10.

Equation 3.16 was discretized for steady state ($\frac{\partial T}{\partial t} = 0$) resulting in

$$
\begin{aligned}
0 \quad = \quad & V_i f_i \rho_{U,i} - A_{i-\frac{1}{2}} \lambda_{i-\frac{1}{2}} \frac{T_i - T_{i-1}}{\frac{1}{2}\Delta r_i + \frac{1}{2}\Delta r_{i-1}} \\
& + A_{i+\frac{1}{2}} \lambda_{i+\frac{1}{2}} \frac{T_{i+1} - T_i}{\frac{1}{2}\Delta r_i + \frac{1}{2}\Delta r_{i+1}}
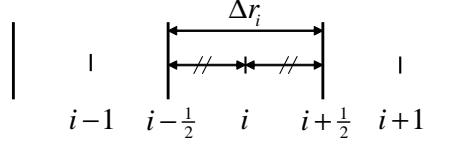\end{aligned}
\qquad (3.40)
$$

Figure 3.10: Locations of volume cell borders and centres.

where V_i is the volume of cell i, $A_{i+\frac{1}{2}}$ is the area of the interface between cell i and $i+1$ and $\lambda_{i+\frac{1}{2}}$ is the thermal conductivity between cell i and $i+1$.

$\lambda_{i+\frac{1}{2}}$ was calculated using the harmonic mean of the heat transfers in cell i and $i+1$, weighted with their cell widths Δr_i, resulting in

$$\lambda_{i+\frac{1}{2}} = \frac{\Delta r_i + \Delta r_{i+1}}{\frac{\Delta r_i}{\lambda_i} + \frac{\Delta r_{i+1}}{\lambda_{i+1}}} \tag{3.41}$$

with λ_i the total thermal conductivity of the fuel gas in cell i.

For cylindrical coordinates, with Δr_i the width of cell i, the following equations can be derived for V_i and $A_{i+\frac{1}{2}}$

$$V_i = \pi r_{i+\frac{1}{2}}^2 - \pi r_{i-\frac{1}{2}}^2 \tag{3.42}$$

$$A_{i+\frac{1}{2}} = 2\pi r_{i+\frac{1}{2}} \tag{3.43}$$

where $r_{i+\frac{1}{2}}$ is the r-coordinate of the boundary between cell i and $i+1$.

Equation 3.40 can be rearranged in a linear set of equations of the form

$$\begin{aligned} V_i f_i \rho_{U,i} = & \left(\frac{2A_{i-\frac{1}{2}}\lambda_{i-\frac{1}{2}}}{\Delta r_i + \Delta r_{i-1}} + \frac{2A_{i+\frac{1}{2}}\lambda_{i+\frac{1}{2}}}{\Delta r_i + \Delta r_{i+1}} \right) T_i \\ & - \left(\frac{2A_{i-\frac{1}{2}}\lambda_{i-\frac{1}{2}}}{\Delta r_i + \Delta r_{i-1}} \right) T_{i-1} - \left(\frac{2A_{i+\frac{1}{2}}\lambda_{i+\frac{1}{2}}}{\Delta r_i + \Delta r_{i+1}} \right) T_{i+1} \end{aligned} \tag{3.44}$$

for $i = 2$ to $n-1$. Using the boundary conditions in equations 3.17 and 3.18 at the centre of the core and at the wall, the heat transfer equations for the first volume cell at $i = 1$ and last volume cell at $i = n$ become

$$V_1 f_1 \rho_{U,1} = \frac{2A_{1+\frac{1}{2}}\lambda_{1+\frac{1}{2}}}{\Delta r_1 + \Delta r_2} T_1 - \frac{2A_{1+\frac{1}{2}}\lambda_{1+\frac{1}{2}}}{\Delta r_1 + \Delta r_2} T_2 \tag{3.45}$$

$$\begin{aligned} V_n f_n \rho_{U,n} = & \left(\frac{2A_{n-\frac{1}{2}}\lambda_{n-\frac{1}{2}}}{\Delta r_n + \Delta r_{n-1}} + \frac{2A_{n+\frac{1}{2}}\lambda_{wall}}{\Delta r_n} \right) T_n \\ & - \left(\frac{2A_{n-\frac{1}{2}}\lambda_{n-\frac{1}{2}}}{\Delta r_n + \Delta r_{n-1}} \right) T_{n-1} - \left(\frac{2A_{n+\frac{1}{2}}\lambda_{wall}}{\Delta r_n} \right) T_{wall} \end{aligned} \tag{3.46}$$

where λ_{wall} is the thermal conductivity of the fuel gas evaluated at $T = T_{wall}$.

The pressure p was calculated using a discretized version of equation 3.12, resulting in

$$p = \frac{N_0 k}{\sum_i \frac{V_i}{T_i g_i}} \tag{3.47}$$

38

Algorithm 1 Layout of the FORTRAN heat transfer program.

```
Input T_wall, n_c, P
DO
  Calculate thermophysical gas properties
  Check for convergence
  Calculate new T
LOOP
Output T(r), ρ(r), p
```

Program overview

The discretized equations were implemented in a FORTRAN program to calculate the radial temperature profile $T(r)$, density profile $\rho(r)$ and pressure p inside the GCR core. As input the code needs the graphite wall temperature T_{wall}, the thermal power P, and the critical density n_c from which the total number of molecules inside the core can be calculated. The temperature field is calculated inside a loop, since almost all thermophysical properties in the heat transfer equation depend on both pressure and temperature. A program layout is depicted in algorithm 1.

Equations 3.40, 3.45 and 3.46 form a set of linear equations and can be written into a matrix equation of the form

$$\mathbf{AT} = \mathbf{B} \tag{3.48}$$

with $\mathbf{A}$ an $n \times n$ diagonal matrix and $\mathbf{T}$ and $\mathbf{B}$ vectors of length n. This matrix equation is solved using a linear solver routine (`dgtsv`) from the lapack library [Anderson,1999].

To solve the temperature distribution, several iterations are performed. The program starts with an initial temperature and pressure guess ($T_0 = T_{wall}$ and $p_0 = 1$ bar). In each iteration, first the dissociation function $g(p_{old}, T_{old})$ is calculated for each cell, using the old pressure and temperature, then the pressure $p(g, T_{old})$ is calculated using the new dissociation function and old temperatures. Next all other thermophysical gas properties are evaluated using the old temperature field and the new dissociation and pressure. These are used to build the matix $\mathbf{A}$ and vector $\mathbf{B}$ in equation 3.48. The new temperature field replaces the old one and is used as input for the next loop, until the convergence criterium is met.

To check for convergence, after recalculating all variables, just before running the solver routine, it is checked how well the old temperature field satisfies the new matrix equation 3.48. When, for all i, the following condition is satisfied

$$\left| \frac{(\mathbf{AT}^{t-1})_i - \mathbf{B}_i}{(\mathbf{AT}^{t-1})_i} \right| < \epsilon \tag{3.49}$$

with $\epsilon = 10^{-7}$ and $\mathbf{T}^{t-1}$ the temperature field calculated in the previous iteration, the calculation is assumed to have converged, and the iteration loop is terminated.
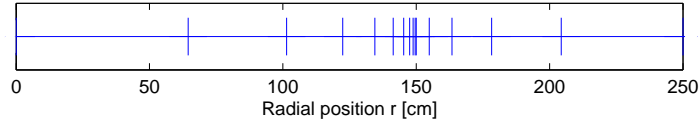
Figure 3.11: Distribution of the course volume zones in GCR cases 2 and 3 in the core ($r < 150$ cm) and the reflector ($r > 150$ cm). Depicted are the boundaries of the course volume zones.

3.5 Volume Cell Distribution

The temperature gradient in a GCR is near the reflector wall several orders larger than in the centre of the core, due to the lower thermal conductivity at the low temperatures near the wall. To be able to calculate the temperature field with sufficient precision, but keep the total number of volume cells manageable, a non-uniform grid is used. We also wanted to use the heat transfer code to do coupled calculations together with MCNP, but in MCNP not as many zones are needed as in the heat transfer code. Thus a non-uniform grid was defined with 10 zones in the fuel gas region and 5 zones in the reflector region, used in the MCNP calculations. In the heat transfer calculations, each zone was split up into m smaller cells with uniform width.

The distribution of the course volume zones is defined using a constant ratio between the widths of adjacent volume zones, such that each zone closer to the wall is $\frac{1}{a}$ times the width of the previous zone. The zone widths ΔR_i were calculated using

$$\Delta R_i = \frac{a^{(n-i)} R_c}{\sum_{j=1}^{j=n} a^{(j-1)}}$$

with i counting from the centre of the core, R_c the radius of the core and n the number of course zones. A ratio of $a = 1.75$ was chosen, resulting in a course volume zone distribution depicted in figure 3.11.

As mentioned above, in the heat transfer code each course zone is split up in m fine cells of uniform width. Cell 1 to m had width $\Delta r_{1..m} = \Delta R_1/m$, the next m cells had width $\Delta r_{m+1..2m} = \Delta R_2/m$, etc., with m equal for all course zones. To determine how many fine cells m are needed per course zone, the temperature profile of core case 2, see table 2.1, with thermal power set to $P = 0.1$ MW, was calculated using different numbers of m, and the resulting temperature profiles were compared. The temperature difference ΔT between calculations using $m = 90$, assuming to be sufficiently accurate, and using $m = 10$ or $m = 2$ fine cells per zone are plotted in figure 3.12. The difference between using 10 or 90 fine cells per zone is less than 1 K at all position, acceptable compared to temperature differences in the thousands of Kelvin. The deviation when using $m = 2$ is over ten times as large, up to 10 K. Thus $m = 10$ is used in the core for temperature calculations. Since temperature gradients are much smaller in the reflector, the error in the temperature is less sensitive to the volume cell width, and in the reflector region $m = 5$ is used.
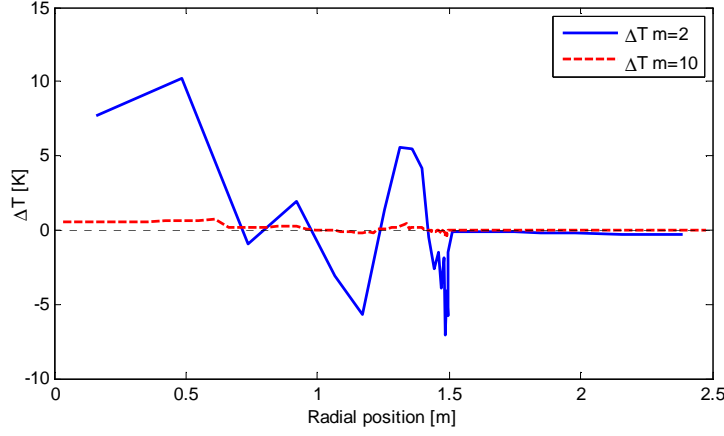
Figure 3.12: Temperature difference ΔT compared to $m = 90$ for calculations using $m = 2$ and $m = 10$ fine cells per zone.

3.6 Code Checks

To check if the calculation of the temperature field was internally consistent, several checks were performed on the calculated heat flows. To perform these checks, the heat flows out of each cell were used. The heat flows towards the left $q_{left,i}$ and towards the right $q_{right,i}$ are calculated for each cell using

$$q_{left,i} = \left(\frac{2A_{i-\frac{1}{2}}\lambda_{i-\frac{1}{2}}}{\Delta r_i + \Delta r_{i-1}} \right) (T_i - T_{i-1}) \tag{3.50}$$

$$q_{right,i} = \left(\frac{2A_{i+\frac{1}{2}}\lambda_{i+\frac{1}{2}}}{\Delta r_i + \Delta r_{i+1}} \right) (T_i - T_{i+1}) \tag{3.51}$$

First it was checked whether the heat balance for each cell was consistent. In steady state, the heat flow out of each cell must be equal to the heat production in that cell. This was done with the following equation

$$V_i f_i \rho_{U,i} = q_{right,i} + q_{left,i} \tag{3.52}$$

Next it was checked that the heat flow out of cell i to $i + 1$ was equal to the heat flow into cell $i + 1$ from cell i, in other words that the matrix $\mathbf{A}$ was symmetric, using

$$q_{left,i} = -q_{right,i-1} \tag{3.53}$$

Since the first condition is equal to the convergence criterion, and the second condition follows directly from using the same variables in the code to calculate the two heat flows, it was no surprise these conditions were met.

The third check was on the total heat flowing out of each cell in the direction of the wall, $q_{left,i}$. At steady state, for each cell this heat flow must equal the heat produced in the cell itself, plus the sum of the heat produced in all previous cells

$$q_{left,i} = \sum_{j=1}^{j=i} V_j f_j \rho_{U,j} \tag{3.54}$$

41

For the last cell, $i = n$, the total heat flowing out to the reflector must of course equal the thermal power P. Equation 3.54 was also satisfied for all fuel cells.

3.7 Benchmark Calculation

The heat transfer model was validated by duplicating calculations done by van Dam and Hoogenboom [1983] on a spherical GCR. Although the rest of this thesis covers cylindrical models, in van Dam and Hoogenboom heat transfer calculations were only performed on a cylindrical one-dimensional core model, which is why this benchmark covers a spherical one-dimensional GCR core.

In van Dam and Hoogenboom dissociation was ignored and only radiative heat transfer was included. The kinetic heat transfer was assumed to be negligible compared to the radiative heat transfer. To compare the results in van Dam and Hoogenboom with our model, the dissociation function was set to unity ($g = 1$) and the kinetic heat transfer to zero ($\lambda_{kin} = 0$) for all p, T. The resulting pressure p, the maximum temperature T_{max} (at $r = 0$), and the 'effective temperature' $\widetilde{T}$ were calculated. $\widetilde{T}$ was defined in van Dam and Hoogenboom as the hypothetical uniform core temperature, which would give the correct pressure for a given total number of molecules N_{tot}, satisfying

$$p = \frac{N_{tot}}{V} k \tilde{T} \tag{3.55}$$

As input data were used, a core radius of $R_c = 2$ m, 50% enriched uranium and a critical inventory of 58.1 kg Uranium resulting in a total number of molecules of $N_{tot} = 2.113 \times 10^{26}$ molecules. The gas mixture consisted of 70% UF$_4$ and 30% CF$_4$ (molar percentage). The temperature of the inner reflector wall was $T_{wall} = 2500$ K. The spherical geometry of the GCR model changes the values for V and A to

$$V_i = \frac{4}{3}\pi \left(r_{i+\frac{1}{2}}^3 - r_{i-\frac{1}{2}}^3 \right) \tag{3.56}$$

$$A_{i+\frac{1}{2}} = 4\pi r_{i+\frac{1}{2}}^2 \tag{3.57}$$

Temperature profiles were calculated for various values of the reactor power P. The resulting pressure p, maximum temperature T_0, and effective temperature $\widetilde{T}$ were compared with values from van Dam and Hoogenboom. Results are in table 3.1. The calculated values are in excellent agreement with the reference values.

Next, for $P = 0.5$ MW, a new calculation was performed, but now including dissociation and kinetic heat transfer. This was compared with results from the previous calculations, without dissociation and kinetic heat transfer, to investigate the importance of these effects. The resulting density distributions (both particle and uranium atom density per m^3) and thermal conductivities are plotted in figure 3.13 for both calculations. The calculated temperature distributions are plotted in figure 3.14. A comparison of the maximum temperature T_{max}, effective temperature $\widetilde{T}$, average fuel mass tempearture $\bar{T}_m$ and pressure p is given in table 3.2.

There is almost no difference in the maximum temperature T_{max} at $r = 0$. The pressure however is more than a factor two higher when including dissociation and λ_{kin}. This is due to dissociation effects, resulting in an increase in

Table 3.1: Comparison of maximum fuel temperature T_{max}, effective temperature $\widetilde{T}$, and core pressure p calculated by the heat transfer code (-cal) with values from van Dam and Hoogenboom [1983].

P [MW]	T_{max} [K]	T_{max}-cal [K]	$\widetilde{T}$ [K]	$\widetilde{T}$ -cal [K]	p [bar]	p-cal [bar]
0.1	4440	4445	3580	3604	3.12	3.14
0.5	6450	6447	5020	5025	4.38	4.38
2.0	9050	9057	6980	6977	6.08	6.07
10.0	13510	13505	10370	10365	9.03	9.03
50.0	20190	20200	15480	15498	13.5	13.5
100.0	24010	24021	18410	18440	16.0	16.1

Table 3.2: Temperatures (maximum T_{max}, effective $\widetilde{T}$ and mass averaged $\bar{T}_m$) and pressure p for a spherical GCR ignoring dissociation g and kinetic heat transfer λ_{kin} (as in van Dam and Hoogenboom), and when including dissociation and kinetic heat transfer in the calculations.

Variable	$g = 1$ $\lambda_{kin} = 0$	$g = f(p,T)$ $\lambda_{kin} = f(p,T)$
T_n [K]	6448	6447
$\widetilde{T}$ [K]	5027	4897
$\bar{T}_m$ [K]	5027	4482
p [bar]	4.38	10.62

the total number of particles in the GCR core. The 'effective' temperature $\widetilde{T}$, as defined in equation 3.55, has no real meaning when dissociation is included, but the mass averaged fuel temperature $\bar{T}_m$ does, as it describes the neutronics of the fuel. $\bar{T}_m$ is significantly lower in the case including dissociation, due to a more extreme density redistribution towards the wall, together with a lower temperature in this region due to a higher λ_{tot} with the inclusion of λ_{kin}. This can also be seen from figure 3.13. The molecular density n is a constant factor higher throughout the core due to dissociation. However, the uranium atom density n_U, proportional to the actual mass density ρ of the fuel, is higher near the wall, and a lot lower near the centre. This results in more mass in the 'colder' region near the wall, and thus a lower mass averaged temperature $\bar{T}_m$.

When examining the heat transfer for the two cases, we see a significantly lower radiative thermal conductivity λ_r due to the higher particle density n when dissociation is included. However, close to the wall the contribution of the kinetic thermal conductivity λ_{kin} becomes more important and causes the total conductivity to be higher than in the case where λ_{kin} is ignored. This causes temperatures near the wall to be lower (see figure 3.14), but when coming closer to the centre, the lower radiative thermal conductivity causes a faster rise of the temperature towards the centre resulting in almost equal maximum temperatures T_{max}. From the plot of the thermal conductivities one would perhaps expect a much higher temperature near the centre for the case including dissociation and λ_{kin}, because λ_{tot} is only in a small region slightly higher. But this small region is also the region were λ_{tot} is very low, and thus the most important for the heat transfer towards the wall away from the central region.
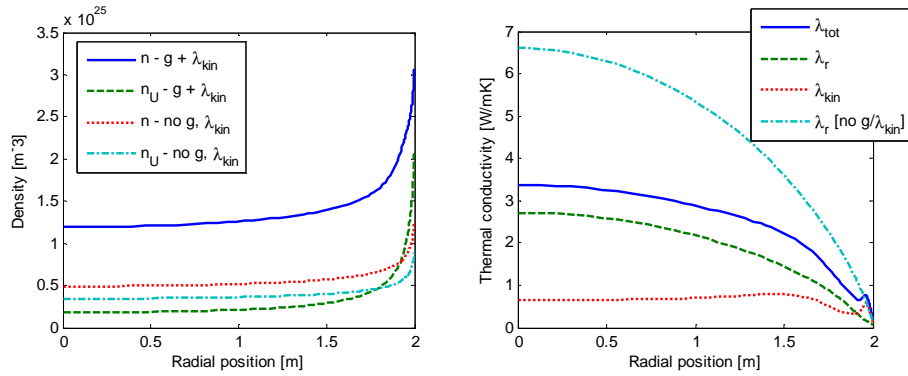
Figure 3.13: Comparison of the fuel particle density n in molecules/m^3 and uranium atom density n_U in uranium atoms/m^3 (left) and radiative λ_r, kinetic λ_{kin} and total λ_{tot} thermal conductivities (right) for calculations with and without dissociation and kinetic heat transfer.
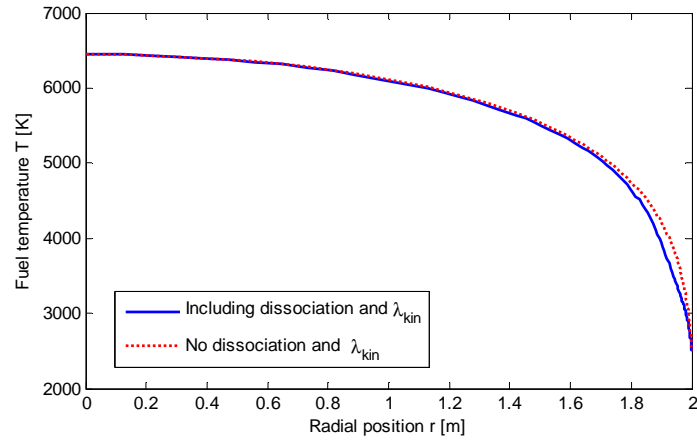

Figure 3.14: Fuel temperature profiles inside a spherical GCR when dissociation and kinetic heat transfer is included in the calculations and when they are ignored (as in van Dam and Hoogenboom).

Algorithm 2 Adjusted heat transfer program, using the average fuel temperature T_f as input, calculating besides the radial temperature and density distributions also the thermal power P.

```
Input T_f, T_wall, n_c,
DO
   Calculate T(r), ρ(r) (see Algoritm 1)
   Check for convergence
   Adjust P
LOOP
Output T(r), ρ(r), p, P
```

From the benchmark calculations it was concluded that the heat transfer model gave results in excellent agreement with earlier calculations in van Dam and Hoogenboom [1983], giving confidence in the validity of the heat transfer model. When comparing calculations with and without dissociation and kinetic heat transfer, it is concluded that both dissociation and the kinetic heat transfer play an important role in the heat transfer inside a GCR. The inclusion of dissociation has a great influence on the core pressure p and on the density distribution of the fuel inside the core. The kinetic thermal conductivity has a significant effect on the thermal conductivity near the wall where the fuel temperature is low and radiative heat transfer becomes less effective. Together with the fuel redistribution due to dissociation λ_{kin} significantly lowers the mass average fuel temperature inside the core, for an equal thermal load to the wall.

3.8   Heat Transfer Calculations

Once the heat transfer model was tested and validated, it could be used to calculate the radial temperature $T(r)$ and density distribution $\rho(r)$ for each of the three cylindrical core cases from table 2.1. These cases were defined by their average fuel temperature T_f and critical density n_c, instead of their power P. Since the effect of changing the fuel or density distribution in a GCR is expected to have only minor effects on the criticality, we assumed any temperature and density profile which has average fuel temperature T_f and average density n_c will satisfy a critical reactor. To calculate these profiles, the heat transfer program was adapted to use the average fuel temperature T_f as input parameter instead of the thermal power P.

The heat transfer code was adjusted to seek the thermal power P for which the resulting temperature $T(r)$ and density profile $\rho(r)$ would result in a mass averaged fuel temperature $\bar{T}_m$ equal to T_f, using T_f, T_{wall} and n_c as input parameters. This was done by adding a second loop around the loop from algorithm 1, in which the power P was adjusted and a new temperature distribution calculated until the difference between the calculated $\bar{T}_m$ and input value T_f, $|\bar{T}_m - T_f|$, was less than 0.5 K, see algorithm 2. Besides the radial temperature and density distributions and thermal reactor power P, also the core pressure p was calculated.

For each case, input values for the critical density n_c, the average fuel temperature T_f and the core radius R_c were taken from table 2.1 and 2.2. The input value for the inner reflector wall temperature was $T_w = 2000$ K and a flat

Table 3.3: For each case the critical fuel density n_c and average fuel temperature T_f are given which were used as input, together with the calculated thermal power P, pressure p and maximum fuel temperature T_{max}.

|	n_c [atoms/b-cm]	T_f [K]	P [kW]	p [bar]	T_{max} [K]
Case 1	3.18×10^{-5}	10000	962.2	48.98	14624
Case 2	2.833×10^{-5}	4400	104.4	8.477	6048
Case 3	4.37×10^{-4}	4400	40.5	96.84	6369

specific power density $f(r) = 1$ was assumed. A comparison with calculations using more detailed neutronics input can be found in chapter 4. The calculated temperature $T(r)$ and density $\rho(r)$ distributions for each case are plotted in figure 3.15. The resulting thermal power P, core pressure p and maximum fuel temperature T_{max} in the centre of the core are listed in table 3.3.

When comparing the core pressures in table 3.3 with those in 2.2, the calculated pressure is two times higher for case 3, three times for case 2 and even five times higher for case 1. These differences result from the fuel gas dissociation, which is more pronounced at lower pressure (case 2) and higher temperature (case 1), see figure 3.2. It is also noted that the core pressure for case 3 is nearly 100 bars, the maximum pressure for which the thermophysical data used in the heat transfer model is still valid.

The differences in the thermal powers P between the three cases is very large. P represents the amount of heat leaving the reactor through the graphite reflector, and depends on the temperature gradient and thermal conductivity λ_{tot} near the wall. As the temperatures are much higher in case 1, so is the temperature gradient, explaining the much higher P. λ_{kin} is lower for higher pressures, and as $\lambda_{kin} > \lambda_r$ near the wall, so is λ_{tot} near the wall, which explains the difference in P between case 2 and 3. Due to the lower fuel density in case 2, λ_r is higher than in case 3. This results in a flatter temperature distribution in the central part of the core, where the radiative heat transfer is more important, which is why the maximum fuel temperature T_{max} is lower for case 2 than for case 3. See also figure 3.15.

As can be seen from figure 3.15 all three cases have steep temperature gradients near the wall, due to the lower temperatures near the wall, resulting in a low λ_r. This same steep temperature gradient is the cause of the sudden increase in the fuel gas density $\rho(r)$ near the wall. As the temperature drops nearer to the wall, not only does the particle density increase according to the ideal gas law, but the fuel gas also recombines into larger, heavier molecules, resulting in a sudden, extreme rise in density. Thus the density difference between the core centre and close to the graphite wall is a factor 40 for case 1, where dissociation is most pronounced due to the very high temperatures, and a factor 10 for cases 2 and 3, much higher than would be expected without dissociation.

Also depicted in figure 3.15 is the temperature profile inside the graphite reflector, based on equation 3.19, and a heat flux through the reflector equal to the thermal power P. As can be seen, the temperature profile inside the reflector drops off faster for case 1 than for cases 2 and 3. This is mostly due to the higher thermal power inside the core, requiring a larger temperature difference to sustain an equal heat flux through the reflector, but also due to the smaller
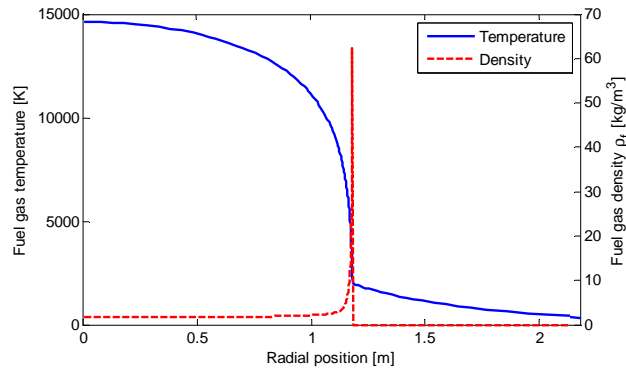
(a) Case 1
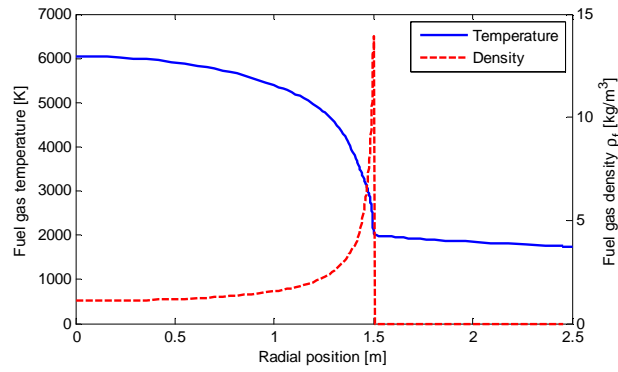
(b) Case 2
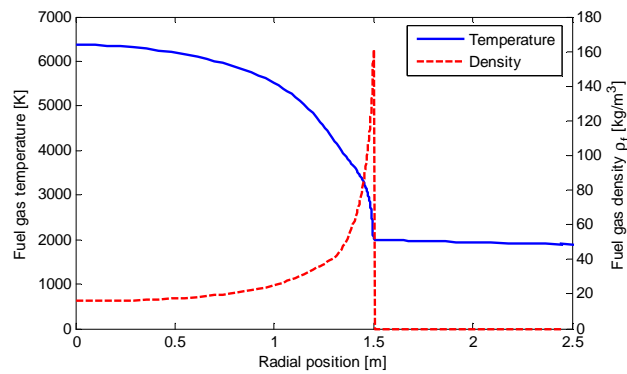
(c) Case 3

Figure 3.15: Calculated temperature $T(r)$ profile and fuel density $\rho(r)$ for the three cylindrical cases describe in table 2.1.

core size, resulting in a smaller graphite surface through which the heat flux can flow. As can be seen in figure 3.15, the average reflector temperature was around 1900 K for cases 2 and 3, based on which the average reflector temperature T_r was chosen to be 1900 K for these cases, as mentioned in chapter 2.

3.9   Conclusions

A heat transfer code was developed which accurately describes the temperature and denstity distributions inside a GCR, under the assumptions detailed in section 3.1. The code was thoroughly tested with internal checks, and gave results in excellent agreement with results from van Dam and Hoogenboom [1983] in benchmark calculations in section 3.7, giving us confidence in results calculated with the code.

Due to the high fuel temperatures, radiative heat transfer is important in a GCR. Radiative heat transfer can be modelled using the Rosseland diffusion approximation, as for all critical fuel densities inside a GCR core the photon mean-free-path length will be much smaller than the core radius. Since the radiative thermal conductivity λ_r scales with T^3, λ_r is small near the core wall where temperatures are low, resulting in a steep temperature gradient. Further away from the wall, where temperature are higher, λ_r is large, resulting in a flat temperature distribution in the central part of the core.

In section 3.7 a comparison of calculations with and without dissocation and kinetic heat transfer showed both are of importance in heat transfer calculations inside a GCR. Due to dissociation, the pressure inside a GCR will be a factor two or more higher for moderate fuel temperatures of 4400 K than would be expected without. For higher fuel temperatures the effect is even more pronounced. Another effect of the dissociation of the fuel gas is a more extreme density redistribution towards the wall, due to dissociation of the fuel gas in the central region of the core.

Although the kinetic thermal conductivity λ_{kin} is smaller than λ_r in most of the GCR core, near the wall $\lambda_{kin} > \lambda_r$. Thus the inclusion of λ_{kin} will cause a significant increase in λ_{tot} near the wall, lowering the temperature gradient near the wall. Together with the extreme density redistribution towards the wall due to dissociation, the higher thermal conductivity near the wall causes a significant decrease of the average fuel temperature when keeping the thermal load to the wall the same. In the benchmark calculations a difference in the average fuel temperature of 600 K was observed.

When examining the calculation results for the three core cases, results of the heat transfer for core cases 2 and 3 are within limits of the core model. However, results for case 1 are not valid as temperatures are well above 10000 K in a large region of the core, beyond the validity of the data describing the properties of the fuel gas. Also at these temperatures significant ionization of the fuel gas will occur, causing the fuel gas to form a (partial) plasma, and the ideal gas law is no longer valid under these conditions.

From results for cases 2 and 3 it can be concluded, that, for an equal average fuel temperature, a higher fuel density will result in a lower thermal load to the wall, as radiative and kinetic heat transfer become less effective at higher pressures. For case 3, using low enriched fuel and having a high density, for an average fuel temperature of 4400 K, the thermal load to the wall was only 40 kW

per meter length of the cylinder. For a cylinder with a diameter of 1.5 meters this translates to a flux to the graphite wall of only 5.7 kW/m^2. However, the higher density due to the low enriched fuel of case 3 results in a pressure of nearly 100 bars at a fuel temperature of 4400 K, limiting the operating temperature of the fuel gas for low enriched uranium.

Chapter 4

Coupled Heat Transfer and Neutronics

In most research on GCRs, either neutronics calculations are performed assuming a uniform temperature and density field inside the core, or the heat transfer is investigated assuming a flat neutron flux and specific power density. In this chapter the errors caused by these assumptions are investigated. Effects of the coupling between heat transfer and neutronics are also of interest in transient calculations, in which the effects of changing temperature or density profiles is important.

The same three GCR core cases as in table 2.1 were investigated. First, the coupling of the heat tranfer code with neutronics calculations using MCNP is explained, and how a converged solution was reached. Coupled calculations were performed for the three core cases, and results for the specific power density $f(r)$, the heat transfer inside the core, and the multiplication factor were compared with neutronics results using uniform temperature and density profiles from chapter 2, and heat transfer results using a uniform specific power density from chapter 3.

4.1 Coupled Calculation

In this section it is explained how calculations with the heat transfer code were coupled with neutronics calculations using MCNP. The goal of the coupled calculations for the neutronics was to investigate the effect on k_{eff} and $f(r)$ of using calculated temperature and density profiles $T(r)$ and $\rho(r)$ in the MCNP calculations instead of assuming a uniform T and ρ, and to find the effect on $T(r)$, $\rho(r)$, P, and p of using the calculated $f(r)$ instead of assuming $f(r) = 1$ in the heat transfer calculations.

For precise calculations, the heat transfer code requires information about the shape of the specific power density $f(r)$ from neutronics calculations. On the other hand, the neutronics calculations with MCNP needs information on the fuel density and temperature distribution inside the core. To find a converged solution for these profiles, the heat transfer and neutronics calculations were coupled in an iterative loop, see figure 4.1. The same heat transfer code as explained in algorithm 2 is used. As input for the coupled calculations, the

desired average fuel temperature $\bar{T}_f$, the inner graphite wall temperature T_{wall}, the critical density n_c and the reflector bulk temperature T_r are used.

The heat transfer code uses $\bar{T}_f$, T_{wall} and n_c as input, together with the newest specific power density $f(r)$, to calculate a temperature and density profile, $T(r)$ and $\rho(r)$, together with the thermal power P and pressure p, for which the mass average fuel temperature $\bar{T}_m = \bar{T}_f$.

The calculated $T(r)$ and $\rho(r)$ are used as input in the MCNP calculations, averaged over the course volume zones used in MCNP, together with the bulk reflector temperature T_r for the reflector temperature. See figure 4.2 for an example of the calculated density profile $\rho(r)$ by the heat transfer code, with its corresponding density distribution in MCNP. MCNP gives as output a new specific power density profile $f(r)$, which is used as input for the next heat transfer calculation until the calculations are converged.

To check for convergence, the new specific power profile is compared with the old $f(r)$ and if the relative change in the specific power profile, $\left| \frac{f_{new}(r) - f(r)}{f(r)} \right|$, is less than a convergence limit ε for all volume zones, the calculation is converged.

The converged solution is used as input for a final, longer MCNP run, to calculate the multiplication factor k_{eff} with large precision. This k_{eff} can be compared with k_{eff} calculated in table 2.2 for a flat temperature and denstiy profile, to estimate the effect of fuel and temperature redistribution inside a GCR.

In the coupled calculation, $k_{eff} = 1$ was not used as convergence criteria, as changes in k_{eff} due to changing density and temperature profiles are very small, and it takes a long time to calculate k_{eff} to a large precision with MCNP. Instead, a converged solution for the specific density $f(r)$ was sought, since this can be calculated relatively fast with large enough precision. The MCNP short run in which $f(r)$ is calculated was 250 cycles with 16000 source particles, while the long MCNP run to calculate k_{eff} with enough precision was 1000 cycles with 75000 source particles, almost 20 times longer.

4.2 Coupled Calculation Results

For each case from table 2.1, the coupled heat transfer and neutronics calculations were performed. For the input values for $\bar{T}_f$ and T_r, the fuel temperature T_f and reflector temperature T_r from table 2.1 were used. For n_c the critical density n_c from table 2.2 was used and for the wall temperature $T_{wall} = 2000$ K. For the first heat transfer calculation, as initial guess of the specific power density, the $f(r)$ calculated in chapter 2 was used. The calculations were converged if the change in specific power was less than $\varepsilon = 0.1\%$. For each case it took only two iterations for the specific power density to converge. Results for the coupled heat transfer and neutronics after convergence of the specific power density are given in the sections below.

4.2.1 Specific Power Density

The calculated specific power density $f(r)$ from the coupled calculations for each of the three core cases is plotted in figure 4.3. As can be seen when comparing the plots with the specific power density for a uniform mass and temperature
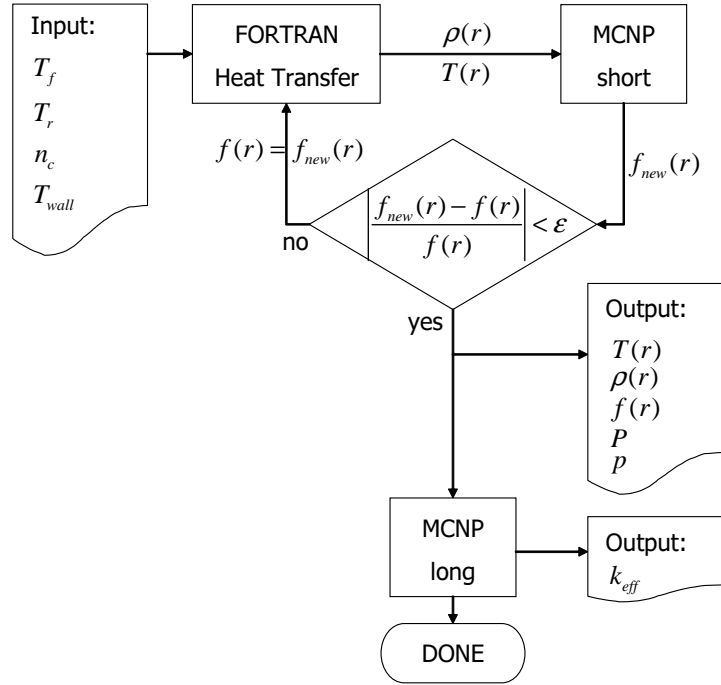
Figure 4.1: Flow chart of the coupled heat transfer and neutronics calculation.
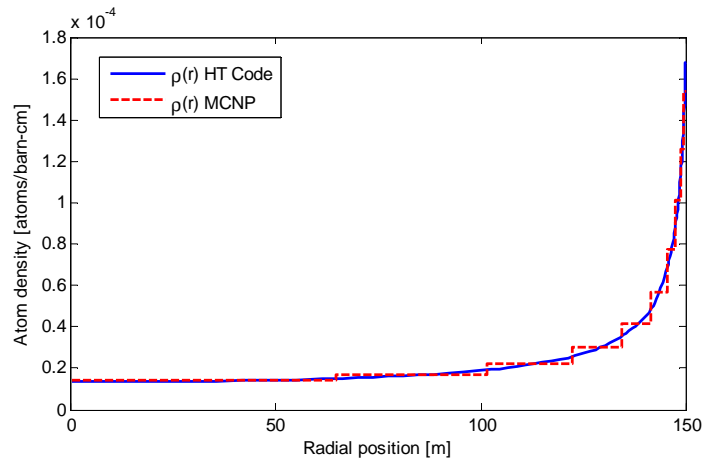

Figure 4.2: Fuel density distribution in atoms/barn-cm as calculated by the heat transfer code and the corresponding fuel density distribution used as input in MCNP for case 2.
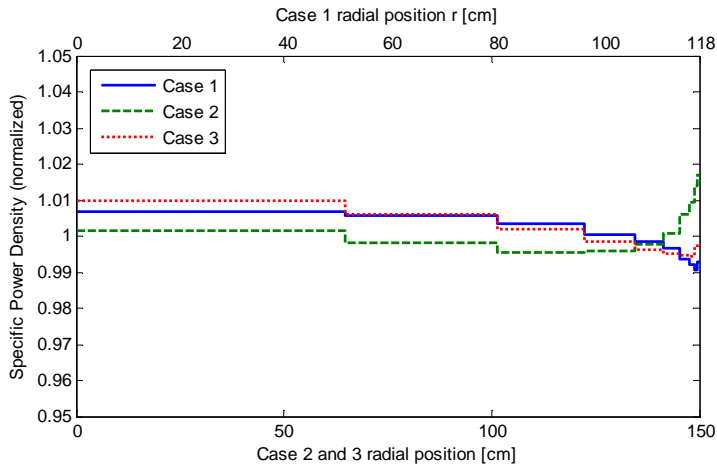
Figure 4.3: Normalized specific power density $f(r)$ for each case, for the coupled calculations. The r-coordinate of case 1 is on the top x-axis, the values on the bottom axis refer to case 2 and 3.

distribution from figure 2.2, the fuel density redistribution has a noticable effect on the specific power density profiles.

For case 1 and case 3 there is a clear drop in the specific power density close to the reflector wall compared to $f(r)$ for uniform temperature and density distributions. This is caused by increased absorption and scattering of neutrons near the wall, due to the high fuel density near the wall, see figure 3.15.

For case 2, the shape of $f(r)$ changed slightly, but the difference between the centre and next to the wall remained around 2%. Even after fuel redistribution, the gas densities near the wall where not dense enough to have a significant impact on the specific power density.

When comparing the specific power densities for the coupled calculations in figure 4.3 with $f(r)$ calculated for a uniform temperature and density in figure 2.2, the already small differences between the maximum and minimum value of $f(r)$ are even smaller when density and temperature distributions are taken into account. Differences were below 2% for all core cases, indicating a flat specific power profile $f(r) = 1$ is a good approximation for all GCR cores.

4.2.2 Heat Transfer

Heat transfer calculations for the coupled calculations, using the converged specific power density, resulted in no noticable difference in the temperature and density distributions compared to the heat transfer equations in section 3.8, where a uniform specific power density of $f(r) = 1$ was used. The power, pressure and maximum temperature for the three cases were also calculated and compared with results from the uncoupled calculations, see table 4.1. As can be seen, there is also no significant difference in these quantities between the coupled and uncoupled results.

Initially, the effect of using a coupling between the neutronics and the thermohydraulics was expected to have a minor, but noticable effect on the heat transfer, since the specific power density calculated in chapter 2, figure 2.2, had

Table 4.1: Results for the coupled calculations of the thermal power P, pressure p and maximum temperature T_{max} for each case, together with the uncoupled results from table 3.3.

	Uncoupled			Coupled		
	P [kW]	p [bar]	T_{max} [K]	P [kW]	p [bar]	T_{max} [K]
Case 1	962	49.0	14624	960	49.0	14631
Case 2	104	8.48	6048	104	8.48	6052
Case 3	40.5	96.8	6369	40.6	96.8	6370

a small deviation between the centre of the core and the wall of up to 6% for case 3. However, as seen in the previous paragraph, the specific power density flattens out when calculated for the real density distribution, resulting in an almost constant value. With these results in mind it is no surprise that the heat transfer calculations resulted in equal temperature and density distributions as for the uncoupled case, where a uniform specific power density of $f(r) = 1$ was used. It is concluded that using a flat specific power density is a good approximation in heat transfer calculations in a GCR, for all fuel densities and enrichments, and will lead to no significant errors.

4.2.3 Reactivity Effect of Fuel and Temperature Redistribution

In this section the effect on the reactivity of using the actual fuel density and temperature distribution compared to using uniform distributions is calculated for each of the three cases.

In van Dam and Hoogenboom [1983] the effect on the reactivity of fuel redistribution towards the wall was also investigated for several one-dimensional core models. The investigated models were a cylindrical core model equal to case 1, and a slab and spherical core. The reacivity effect was calculated by comparing calculations of the multiplication factor for fuel density profiles with higher densities near the wall than near the centre of the core, with calculations with a uniform density distribution. The imposed fuel density profiles were not calculated with heat transfer equations, but analytical functions were used, with two to three times higher densities near the wall than near the centre of the core. A uniform fuel temperature was used and calculations were performed with the deterministic S_n code ANISN.

For the slab core, no reactivity effect of fuel redistribution was found, but for both the cylindrical and spherical reactor a small reactivity effect was calculated. The reactivity effect was calculated to be between 72 and 86 pcm for the cylindrical reactor, using an S_n order of S_4. However, calculations for the spherical reactor core with different S_n orders showed S_4 calculations resulted in a significant overprediction of the reactivity effect of 30 to 40 pcm.

The explanation for the reactivity effect of the fuel redistribution towards the wall was sought in the distribution of the paths neutrons traverse through a GCR in a curved geometry. In a GCR the reflector is the source of thermal neutrons. It can be shown that for neutrons flying along straight, uninterrupted paths through the core, the average path length traversed by neutrons per unit volume, equal to the neutron flux, is larger in a region near the wall than near

54

Table 4.2: Difference in the multiplication factor, compared to calculations using a flat density and temperature profile, for calculations using the calculated density distribution and a uniform fuel temperature, and for calculations using both the calculated density and temperature profile, non-uniform T. The standard deviation of the calculated reactivity change is 13 pcm.

	Uniform T [pcm]	Non-uniform T [pcm]
Case 1	−1	10
Case 2	33	22
Case 3	−1	−12

the centre of the core, in a curved geometry. See appendix B for a mathematical analysis of the distribution of the paths traversed by neutrons through an empty cylindrical core. This means that for neutrons flying in straight uninterrupted lines, an acceptable approximation when $l_t \gg R_c$ and $l_a \gg l_s$, the flux will be higher near the wall than in the centre of the core, and fuel redistribution towards the wall will result in an increase in reactivity.

In our own research, in the calculations of the specific power densities $f(r)$ for uniform density and temperature profiles, see figure 2.2, it was noted that $f(r)$ was slightly higher near the core wall, which indicates a higher probability of fission in the fuel near the wall. In section 2.4 it was mentioned this could indicate a change in the fuel density distribution might lead to an increase in reactivity, as long as the fuel redistribution would not have too big an effect on the specific power density. Since the neutron mean-free-path lengths inside a GCR are large, especially for cases 1 and 2, the effect of redistributing fuel on the specific power profile was expected to be negligible.

In the coupled calculation a converged fuel density distribution $\rho(r)$ and fuel temperature distribution $T(r)$ is calculated for each core case. To investigate both the effect of the fuel density redistribution and of the temperature profile on the reactivity, compared to using flat density and temperature profiles, two criticality calculations were performed with MCNP. One calculation used only the calculated fuel density distribution $\rho(r)$ and a constant fuel temperature of T_f. The second calculation used both $\rho(r)$ and the calculated fuel temperature distribution $T(r)$ as input for the MCNP calculation. For all calculations, a uniform reflector temperature of T_r from table 2.1 was used. For each case the changes in reactivity, compared to the k_{eff}'s calculated in table 2.2 for the uniform temperature and density profiles, were calculated and are listed in table 4.2. The uncertainty of all calculated k_{eff} values is 9 pcm, resulting in a combined uncertainty in the reactivity changes of $\sigma = \sqrt{9^2 + 9^2} = 13$ pcm.

The reference case, case 1, shows no significant reactivity change due to fuel density redistribution. This is not in accordance with results from van Dam and Hoogenboom. To explain this, results for case 2 are used. Case 2 has a similar average fuel density and enrichment as case 1, and shows comparable neutronics behaviour in all calculations in chapter 2. For case 2 however, a significant change in the reactivity due to fuel redistribution is observed of 33 pcm. The difference is that in case 2 the fuel redistribution towards the wall is less extreme than for case 1, see figure 3.15. The difference in densities between the centre and near the wall is a factor 10, instead of 40 for case 1. When

comparing the fuel distribution used in case 1 with the fuel distributions used in van Dam and Hoogenboom, a similar difference is noted, as there the difference in density between the core centre and the wall was at most a factor 2.5. The reactivity change of 33 pcm due to fuel distribution is in accordance with results of van Dam and Hoogenboom, if we take into account the overprediction of the calculated reactivity effect in their results.

Case 3 also showed no significant reactivity change due to fuel redistribution. However, both explanations mentioned above for an increase in the reactivity rely on large neutron mean-free-path lengths inside the core, and a low scattering probability. As was calculated in table 2.3, the mean-free-path lengths in case 3 do not satisfy these conditions. This explains why case 3 does not show any significant change in the reactivity due to fuel redistribution towards the wall.

Using the calculated temperature distribution $T(r)$ instead of a uniform temperature inside the core did not result in any significant reactivity changes. For cases 1 and 2 this is no surprise, since the reactivity coefficient of the fuel temperature α_{Tf} is almost zero. For case 3, α_{Tf} is no longer zero, but still small, and showed a linear behaviour over a large temperature region, see figure 2.4. As the non-thermal neutron mean-free-path length is still large, neutrons travel through the entire core. Thus, the average resonance absorption for fast neutrons will hardly change for different temperature distributions, as long as the average fuel temperature stays the same.

We conclude for a GCR with a low fuel density and high enriched uranium, fuel redistribution towards the wall causes a slight rise in reactivity, as long as the fuel redistribution does not cause fuel densities near the wall to become too high. For low enriched uranium fuel, there is no significant effect of fuel redistribution on the reactivity, due to a higher scattering probability in the fuel. The shape of the radial temperature profile has no significant effect on the reactivity in a GCR due to the small reactivity effect of the fuel temperature. Using a uniform temperature distribution instead of the actual temperature profile will not result in any significant errors in neutronics calculations.

Chapter 5

Conclusions and Discussion

In the first section of this chapter conclusions are drawn from the results in the previous chapters on the important parameters for the neutronics in a GCR, the importance of dissociation and kinetic heat transfer for the heat transfer calculations, stability of the power of a GCR during operation, and the effect of using coupled calculations instead of using uncoupled neutronics and heat transfer equations.

The last section gives a discussion on the validity of the results given the uncertainties and simplifications in the models, together with recommendations for future work.

5.1   Conclusions

The neutronics in a gas core reactor are almost completely determined by the fuel gas density and the reflector temperature. The fuel density has the biggest impact on the criticality, which results in a large reactivity coefficient of the fuel density $\alpha'_n = \frac{n}{k}\frac{\partial k}{\partial n}$. Due to the large neutron mean-free-path lengths in a GCR, the thermal neutron spectrum is entirely determined by the reflector temperature, resulting in a large, negative reactivity coefficient of the reflector temperature α_{Tr}, and a small reactivity coefficient of the fuel temperature α_{Tf}. For a GCR using 50% enriched uranium, $\alpha'_n = 0.31$, $\alpha_{Tr} = -6.7$ pcm/K and $|\alpha_{Tf}| \leq 0.01$ pcm/K was found, compared to $\alpha'_n = 0.18$, $\alpha_{Tr} = -3.9$ pcm/K and $\alpha_{Tf} = -0.3$ pcm/K when using 5% enriched uranium.

Due to the large reactivity coefficient of the fuel density, density fluctuations may cause large reactivity insertions in a GCR. In scenario's involving large reactivity insertions ($> 1\$$) or fuel temperature changes, feedback from the reflector temperature is too slow to counter these problems, due to the low thermal conductivity of the fuel gas and the large bulk of the graphite reflector. Since α_{Tf} is relatively small, countering these kinds of incidents depend on α'_n. As the timescale of a change in density due to a change in temperature is comparable to the neutron prompt removal time in a GCR of 0.003 s, it is unclear whether the density feedback is fast enough to counter these kinds of incidents.

Heat transfer calculations showed that dissociation effects and kinetic heat transfer, besides radiative heat transfer, are both important when calculating

the temperature and density distributions inside a GCR core. In the central region of the core where temperatures are high, λ_r is high and dominates the heat transfer, resulting in a flat temperature profile. Near the wall, where T and λ_r are both low, the kinetic thermal conductivity $\lambda_{kin} > \lambda_r$ and inclusion of λ_{kin} in the heat transfer model causes a decrease of the temperature gradient near the wall. In the benchmark calculation, inclusion of dissociation caused an increase in core pressure of over a factor two, and increased the density difference between the centre of the core and the region near the wall from a factor three to a factor 10. The increased density near the wall, together with the decreased temperature gradient due to the inclusion of λ_{kin}, resulted in a decrease of the average fuel temperature of 600 K.

The coupled calculations showed the specific power density $f(r)$ is almost flat, and using $f(r) = 1$ in heat transfer calculations will cause no significant errors. When using high enriched uranium, density redistribution towards the wall results in a small increase in the reactivity in some cases. However, when using low enriched uranium, the shape of the density distribution has no effect on the reactivity. The shape of the temperature distribution has no effect the reactivity for both high and low enriched uranium

5.2   Discussion and Future Work

The use of an infinite cylinder instead of a finite geometry in the neutronics calcultations is expected to have only minor effects on the reactivity coefficients, as there is little dependence on the actual geometry due to the large mean-free-path of neutrons. The critical density will be higher in a finite geometry though. As the coupled calculations have shown, the results for the neutronics are also valid for non-uniform $T(r)$ and $\rho(r)$ profiles in the fuel. However, as the flux profile in the reflector is not uniform, the reactivity coefficient of the reflector α_{Tr} will depend on the temperature distribution in the reflector. For the calculation of both steady state and slow transients the reflector feedback has to be investigated in more detail, for example by calculating the reactivity coefficient per radial zone in the reflector.

Although it was assumed the differences in atomic ratios would be negligible, the validity of this is unknown. Temperature differences and dissociation effects will cause concentration differences of the various species in the gas mixture, which will lead to transport of the various species. The the resulting differences in the local atomic ratios are not easy to estimate without further research.

The large uncertainty in the photon cross section σ_{ph} is expected to lead to only small errors in the temperature profile. Since the temperature gradient is small near the centre of the core, changes in σ_{ph} will have only a small effect on the temperature profile in this region, and near the wall $\lambda_{kin} > \lambda_r$.

Pressure differences in the radial direction are expected to be small compared to the total pressure, as it is expected the density will adjust quickly to any significant pressure differences. Thus, the assumption of uniform pressure is expected to be accurate.

However, the exclusion of fuel flow in the heat transfer model does lead to large errors. The turbulent fuel flow in an operating GCR will significantly increase the heat transfer towards the wall. Also, in a finite cylinder the temperature and density profiles will not be fully developed, but will evolve along

the direction of the flow, resulting in significant axial temperature and density differences. Thus, the developed heat transfer code is only valid for identifying important parameters and investigating general behaviour, and not for the calculation of the actual temperature and density profiles inside a GCR. Fuel flow through a GCR core will also cause a loss of reactivity, as precursors will be transported out of the core.

In the coupled calculations no dependence of the neutronics was observed on the radial profiles of the temperature and density. These results stay valid in the case of fuel flow and a finite geometry.

For the investigation of transients inside an operating GCR core, a model including the time-dependent coupling between the reactor power, the average fuel temperature, the average fuel density inside the core and the radial temperature distribution inside the reflector should be developed. Since the neutron mean-free-path lengths are large inside a GCR, a point kinetics model of the flux shape should be sufficient to model the neutronics, with the benefit that any reactivity loss due to transport of precursors by the fuel flow can be easily incorporated.

Appendix A

Sample MCNP Input Deck

```
MCNP Input file for GCR generated by FORTRAN code
C    CELL CARDS
101  1 3.18000E-05    -11      IMP:N=1 $ Fuel core
102  2 8.55000E-02    11 -12  IMP:N=1 $ Reflector
103  0                12       IMP:N=0 $ Void outside

C    SURFACE CARDS
11   CZ  118.0
12   CZ  218.0

C    DATA CARDS
KCODE 75000 1.0 30 1000
SDEF POS=0 0 0 AXS=0 0 1 RAD=D1 EXT=0
SI1 = 0 100.0
M1   92235.66c 0.070   $ fraction U235
     92238.66c 0.070   $ fraction U238
      6000.66c 0.060   $ fraction C
      9019.62c 0.800   $ fraction F
M2    6000.66c 1.0
MT2   grph.64t          $ Graphite at 1000 K
TMP  0.8617342E-06
     0.8617342E-07
     0.0
C    TALLY CARDS
 F4:N 101
 FM4  (-1 1 (1))     $ Total cross section
      (-1 1 (-2))    $ absorption
      (-1 1 (18))    $ fission
      (-1 1 (2))     $ Scattering
 SD4  1
 E4  2.38e-6 4.31e-3 1.11e-1 20  $ Energy bins
 F14:N 101
 SD14 1
 E14  2.38e-6 4.31e-3 1.11e-1 20  $ Energy bins
PRDMP 2J 1 1
```

Appendix B

Distribution of Paths Traversed by Neutrons Through an Empty Core

In this appendix a mathematical analysis is given which shows that, in a cylindrical core, the average neutron track length per unit volume is larger near the wall of a cylindrical core near the centre of the core, assuming neutrons move in straight, uninterrupted lines from the reflector through the core.

Assuming the core is an infinite cylinder with radius $R = 1$, we can split up the core cavity into two concentric areas with equal surface, one central part and one part near the border, labelled surfaces A (central part) and B (near the wall) in figure B.1, with $r = \frac{1}{2}\sqrt{2}$ the coordinate of the border between A and B that satisfies the condition of surfaces A and B having the same area.

The line that describes the neutron tracks exiting the reflector with angle α with respect to the reflector surface, is given by

$$y = 1 + x \tan \alpha \tag{B.1}$$

with $0 < \alpha < \pi$, and the centre of the core at the origin ($x = 0$, $y = 0$).

The circle enclosing area B can be expressed as

$$x^2 + y^2 = 1 \tag{B.2}$$

and the circle enclosing area A can be expressed as

$$x^2 + y^2 = r^2 = \frac{1}{2} \tag{B.3}$$

With these three expressions for the borders of areas A and B and the neutron track through the core, one can calculate the intersections of the neutron track with the circles, by using equation B.1 to substitute y in equations B.2 and B.3, and solve for x. The resulting two x-values can be inserted in B.1 to find the y-coordinate of the two intersections. This results in 4 coordinates, $\mathbf{o}_1$, $\mathbf{o}_2$, $\mathbf{i}_1$ and $\mathbf{i}_2$, the intersections with the outer and inner circles, each a function of the angle α.
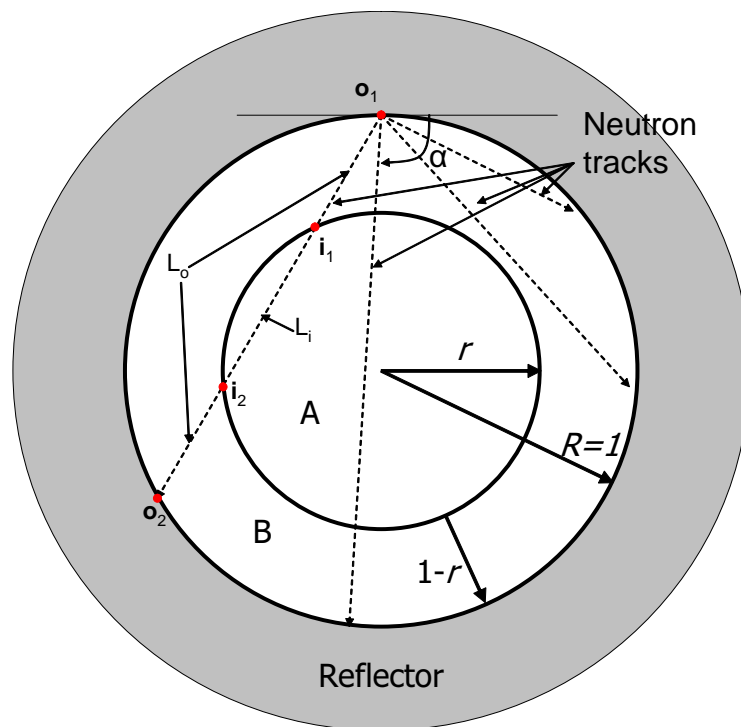
Figure B.1: Neutron tracks leaving the reflector with angle α compared to the reflector surface. Neutrons pass the core through core areas A and B with equal surface area. L_o is the length of a neutron track through the outer area B, and L_i is the length through inner area A.

From these four coordinates, the length of the neutron track through each area can be found, by substracting the two points and taking the length of the resulting vectors.

$$L_i(\alpha) = |\mathbf{i}_1 - \mathbf{i}_2| \tag{B.4}$$

$$L_o(\alpha) = |\mathbf{o}_1 - \mathbf{o}_2| - |\mathbf{i}_1 - \mathbf{i}_2| \tag{B.5}$$

with $L_i(\alpha)$ the length of the neutron track through the inner core area A, and $L_o(\alpha)$ the length of the neutron track through the outer area B.

If we assume the angle α at which neutrons leave the reflector is distributed uniformly, the average neutron track length through the inner area A, and through the outer area B can now be calculate by integrating the track lengths $L_i(\alpha)$ and $L_o(\alpha)$ over α

$$L_A = \int_0^\pi L_i(\alpha)d\alpha \tag{B.6}$$

$$L_B = \int_0^\pi L_o(\alpha)\,d\alpha \tag{B.7}$$

with L_A the average neutron track length through area A and L_B the average neutron track length through area B, in arbitrary units.

With maple it was calculated that the resulting average track lengths through both areas are

$$L_A = 1.694$$
$$L_B = 2.306$$

which proves that the average neutron track length through the outer ring of the core is larger than through the central part of the core, if neutrons can be assumed to move in straight lines through the core and neutrons enter the core from the reflector with a uniformly distributed angle α.

Appendix C

Radial Flux Profiles

The radial flux profiles were calculated with MCNP for the four energy groups, with upper energy bounds of 2.38 eV, 4.3 keV, 111 keV and 20 MeV. Plots are given in figures C.1 to C.3.
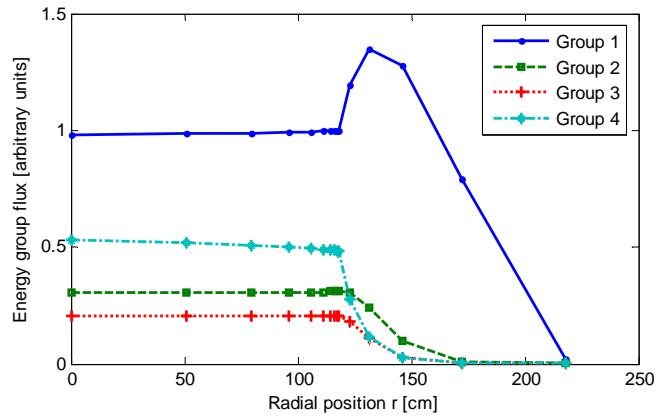
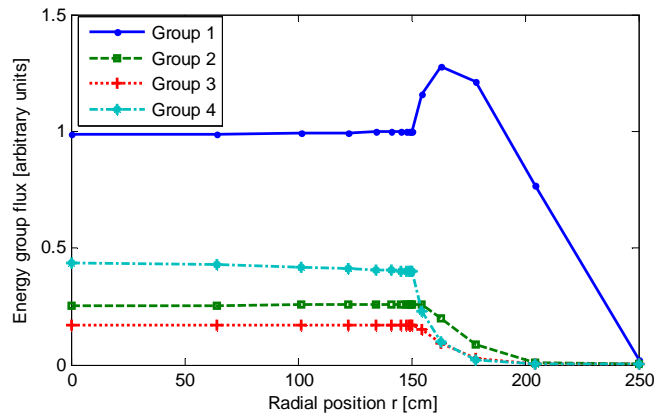Figure C.1: Radial flux profiles for the four energy groups for core case 1.

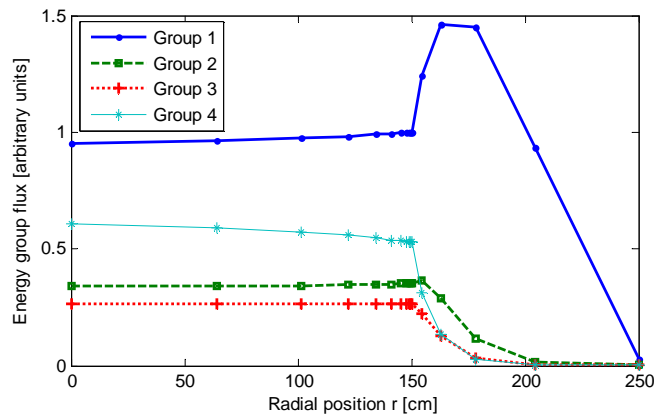Figure C.2: Radial flux profiles for the four energy groups for core case 2.

Figure C.3: Radial flux profiles for the four energy groups for core case 3.

Bibliography

[Anderson,1999]   E. Anderson et al., LAPACK Users' Guide third edition, Society for Industrial and Applied Mathematics, Philidelphia, PA, 1999

[Anghaie,2002]   S. Anghaie, Generation IV Roadmap: R&D Scope Report for Nonclassical Reactor Systems, GIF-006-00, 2002.

[Anghaie,2005]   S. Anghaie, T. W. Knight, R. Norring, B. M. Smith, Optimum Utilization of Nuclear Fuel with Gas and Vapor Core Reactors, Progress in Nuclear Energy 47, pp. 74-90, 2005.

[Bitteker,1993]   L. Bitteker, Determination of the Nuclear-induced Electrical Conductivity in a Nuclear-driven MHD Device, Proceedings of the 29th Intersociety Energy Conversion Engineering Conference, vol. 2 pp. 991-996, 1993.

[Brown,2002]   L. C. Brown et al., Nuclear Production of Hydrogen Using Thermochemical Water-Splitting Cycles, Proceedings of the International Congress on Advanced Nuclear Power Plants, ICAPP 2002, Hollywood, Florida, 2002.

[van Dam,1983]   H. van Dam, J. E. Hoogenboom, Physics of a Gaseous Core Reactor, Nuclear Technology 63, pp. 359-368, 1983.

[Diaz,1993]   N. J. Diaz, Y. Watanabe, E. T. Dugan, Gas/Vapor Core Reactor Heat Transfer Issues, AIChE Symposium Series, Heat Transfer 89, pp. 473-479, 1993.

[Dugan,1989]   E. T. Dugan, G. E. Welch, S. Kahook, Ultrahigh Temperature Vapor Core Nuclear Reactor/MHD Generator Rankine Cycle Space Power System, Proceedings of the 24th IECEC, IECEC 89, pp. 495-500, 1989.

[Duderstadt,1976] J. J. Duderstadt, L. J. Hamilton, Nuclear Reactor Analysis, John Wiley & Sons, ISBN 0-471-22363-8, 1976.

[Dugan,1993]   E. T. Dugan, K. Kutikkad, Reactor Dynamics and Stability Analysis of a Burst-Mode Gas Core Reactor, Brayton Cycle Space Power System, Nuclear Technology 103, pp. 473-479, 1993.

[Kistemaker,1978] J. Kistemaker, Some Aspects of a Fission Based Plasma Engine, Proc. 1st Int. Symp. Nuclear Induced Plasmas and Nuclear Pumped Lasers, Les Editions de Physique, Orsay, 1978.

[Klein,1987] W. Klein, Thermodynamic Performance of a Gas-Core Fission Reactor, PhD Thesis, TU Delft, 1987.

[Klein,1989] W. Boersma-Klein, J. Kistemaker, H. N. Stein, Use of Thermochemical Modelling for the Analysis of Energy Extraction in a Gas-Core Fission Reactor, Journal of Nuclear Materials 167, pp. 135-144, 1989.

[Klein,1991a] W. Boersma-Klein, J. Kistemaker, H. N. Stein, Equation of State and Specific Heats of U-C-F Gas Mixtures, Journal of Nuclear Materials 182, pp. 11-23, 1991.

[Klein,1991b] W. Boersma-Klein, J. Kistemaker, Transport Phenomena in a Dissociating U-C-F Gas Mixture, Journal of Nuclear Materials 182, pp. 24-35, 1991.

[Kuijper,1992] J. Kuijper, A Calculational Study on Neutron Kinetics and Thermodynamics of a Gaseous Core Fission Reactor, PhD Thesis, TU Delft, 1992.

[Lide,2001] D. R. Lide, Editor, Handbook of Chemistry and Physics 82nd edition, CRC Press, 2001.

[Modest,1993] M. Modest, Radiative Heat Transfer, Academic Press, 1993.

[Los Alamos,2003] X-5 Monte Carlo Team, MCNP - A General Monte Carlo N-Particle Transport Code, Version 5, Los Alamos Report, LA-UR-03-1987, Los Alamos National Laboratory, 2003.

[Panicker,1990] M. M. Panicker, E. T. Dugan, Static and Dynamic Neutron Analysis of a Bimodal Gaseous Core Reactor System for Space Power, Proceedings of the 25th Intersociety Energy Conversion Engineering Conference, pp. 150-155, 1990.

[Rohsenow,1973] W.M.Rohsenow, J. P. Hartnett, Handbook of Heat Transfer, McGraw-Hill, 1973.

[Watanabe,1993] Y. Watanabe and S Anghaie, Thermophysical Properties of Gas Phase Uranium Tetrafluoride, AIAA 28th Thermophysics Conference, AIAA 93-2758, Orlando Florida, 1993.